Received: 18 June 2024 | Revised: 27 October 2024 | Accepted: 6 November 2024

DOI: 10.1002/dep2.321

The Depositional Record
Open Access
A journal of the International Association of Sedimentologists
WILEY

ORIGINAL ARTICLE

Smithian–Spathian carbonate geochemistry in the northern Thaynes Group influenced by multiple styles of diagenesis

Jordan P. Todes[1] | **Franziska R. Blattmann**[2,3] | **Torsten Vennemann**[2] | **Elke Schneebeli-Hermann**[4] | **Hugo Bucher**[4] | **Dan P. Razionale**[1,5] | **Clara L. Blättler**[1]

[1]Department of the Geophysical Sciences, University of Chicago, Chicago, Illinois, USA

[2]Institute of Earth Surface Dynamics, University of Lausanne, Lausanne, Switzerland

[3]Department of Geoscience, Aarhus University, Aarhus C, Denmark

[4]Department of Palaeontology, University of Zurich, Zurich, Switzerland

[5]Department of Earth, Environmental and Planetary Science, Brown University, Providence, Rhode Island, USA

Correspondence
Jordan P. Todes, Hinds Geological Laboratory, Department of the Geophysical Sciences, University of Chicago, 5734 S Ellis Ave, Chicago, IL 60637, USA.
Email: jtodes@uchicago.edu

Funding information
Schweizerischer Nationalfonds zur Förderung der Wissenschaftlichen Forschung, Grant/Award Number: 180253; Division of Earth Sciences, Grant/Award Number: 2120406

Abstract

The Smithian–Spathian boundary interval is characterised by a positive carbon isotopic excursion in both $\delta^{13}C_{carb}$ and $\delta^{13}C_{org}$, concurrent with a major marine ecosystem reorganisation and the resurgence of microbialite facies. While these $\delta^{13}C$ records have been traditionally interpreted as capturing global carbon cycle behaviour, recent studies have suggested that at least some excursions in early Triassic $\delta^{13}C$ values may incorporate influences from authigenic or early diagenetic processes. To examine the mechanistic drivers of Smithian–Spathian boundary geochemistry, the carbonate geochemistry of a core from Georgetown, Idaho (USA), was analysed using a coupled $\delta^{44/40}Ca$, $\delta^{26}Mg$ and trace-metal framework. While the $\delta^{13}C$ record in the Georgetown core is broadly similar to other Smithian–Spathian boundary sections, portions of the record coincide with substantial shifts in $\delta^{44/40}Ca$, $\delta^{26}Mg$ and trace-metal compositions that cannot feasibly be interpreted as primary. Furthermore, these geochemical variations correspond with lithology: The $\delta^{13}C$ record is modulated by variations in the extent of dolomitisation, and the diagenetic styles recognised here coincide with individual lithostratigraphic units. A primary shift in local sea water $\delta^{13}C$ values is inferred from the most geochemically unaltered strata, from *ca* 3‰ in the middle Smithian to *ca* 5‰ in the early Spathian, although the timing and pathway through which this occurs cannot be readily identified nor extrapolated globally. Therefore, the Georgetown core may not directly record exogenic carbon cycle evolution, showing that there is a need for the careful reconsideration of the Smithian–Spathian boundary—and more broadly, Early Triassic—geochemical records to examine potential local and diagenetic influences on sedimentary geochemistry.

KEYWORDS

carbon cycle, carbonate diagenesis, dolomitisation, Early Triassic, Smithian–Spathian boundary, Thaynes Group

1 | INTRODUCTION

The aftermath of the end-Permian mass extinction is characterised by substantial fluctuations in the geological carbon cycle: carbonate $\delta^{13}C$ values ($\delta^{13}C_{carb}$) range from −2 to 8‰, among the most extreme instability recognised across the entire Phanerozoic, before stabilising in the Middle Triassic (Payne et al., 2004; Corsetti et al., 2005; Cramer & Jarvis, 2020). As conventionally interpreted, these unusually large and rapid excursions reflect changes in the $\delta^{13}C$ values of dissolved inorganic carbon (DIC) in sea water, possibly linked to pulses of volcanogenic or thermogenic carbon release, variations in the burial flux of organic carbon, unstable carbonate saturation state due to ocean acidification or elevated alkalinity, and/or authigenic carbonate precipitation (Payne et al., 2004; Payne & Kump, 2007; Meyer et al., 2011; Schrag et al., 2013). One of the most prominent of these excursions, the Smithian–Spathian boundary event, is characterised by a pronounced positive excursion in $\delta^{13}C$ values in the Tethyan, Boreal and Panthalassan realms, associated with a major marine biotic crisis, ecosystem reorganisation and episodic marine anoxia (Brayard et al., 2006; Galfetti et al., 2007a, 2007b; Thomazo et al., 2016; Zhang et al., 2019). This excursion has been previously linked with a variety of proposed global palaeoceanographic changes across the Smithian–Spathian boundary interval, including cooling, enhanced organic carbon burial, fluctuations in anoxia and euxinia and variations in carbonate burial (Payne & Kump, 2007; Meyer et al., 2013; Lyu et al., 2019; Song et al., 2019; Zhang et al., 2019; Widmann et al., 2020; Zhao et al., 2020a, 2020b; Ye et al., 2023).

These inferred palaeoceanographic changes across the Smithian–Spathian boundary, as derived from geochemical records, are based on the principles that (i) the studied geochemical proxies record primary oceanographic changes and (ii) the dominant influence on these proxies is global, rather than local or basin-scale dynamics (Galfetti et al., 2007b). However, if Smithian–Spathian boundary geochemical records do indeed capture global, primary geochemical phenomena, then existing records have contradictory implications. For instance, studies have argued for both expanded (Song et al., 2019) and reduced extents of sea floor anoxia and oxygen minimum zones (Lyu et al., 2019; Zhao et al., 2020a) across the Smithian–Spathian transition. In a similar vein, other works have suggested enhanced (Zhao et al., 2020b) and decreased (Song et al., 2021; Ye et al., 2023) carbonate burial across the boundary interval. An alternative to these primary, global mechanisms was proposed by Thomazo et al. (2016, 2019) who, based on records from the North American Thaynes Group, argued that this excursion reflects authigenic carbonate precipitation linked with a regional late Smithian transgressive event—a fundamentally local, post-depositional mechanism. These alternative interpretations suggest that the Smithian–Spathian boundary record may capture varying proportions of global, local and/or diagenetic drivers, each of which would have distinct implications for the extent of environmental perturbation during the Early Triassic. If Smithian–Spathian geochemical archives largely capture global signals, then the sheer magnitude of geochemical change across the boundary interval (3–10‰ excursion in $\delta^{13}C$ values) would suggest that there were profound shifts in the geological carbon cycle—on a par with some of the largest inferred to have occurred throughout the entire Phanerozoic (Payne & Kump, 2007; Meyer et al., 2013; Cramer & Jarvis, 2020). Alternatively, if those same archives are more driven by local and/or post-depositional factors, the Smithian–Spathian boundary may capture an interval of unusual local conditions or post-depositional evolution that, even if found in globally distributed basins, does not necessarily imply that marine geochemistry was uniformly perturbed across the Smithian–Spathian boundary (Thomazo et al., 2016).

A recently drilled core through the Smithian–Spathian boundary succession in the Thaynes Group in Georgetown, Idaho (Schneebeli-Hermann et al., 2020), provides an ideal opportunity to test whether strata in the northern Thaynes Group capture global carbon cycle evolution (Zhao et al., 2020b) or, alternatively, diagenetic overprint (Thomazo et al., 2016). While the organic and carbonate $\delta^{13}C$ records of this core largely match global Smithian–Spathian boundary trends (Schneebeli-Hermann et al., 2020), further work using a carbonate geochemical approach may help decipher the mechanisms driving the preservation of the Georgetown record of $\delta^{13}C$ values. In this study, the Georgetown core is investigated with a multi-proxy geochemical approach ($\delta^{13}C$, $\delta^{18}O$, $\delta^{44/40}Ca$, $\delta^{26}Mg$, trace-metals) to identify local and diagenetic signatures within a defined lithostratigraphic framework. In turn, this enables us to test the specific global and diagenetic hypotheses proposed by previous workers to explain the geochemical expression of the Smithian–Spathian boundary interval. These results suggest that the carbonate geochemistry of the Georgetown core does not reflect either global carbon cycle evolution or authigenic carbonate precipitation, but instead results from a variety of diagenetic mechanisms linked to sedimentological variations.

2 | GEOLOGICAL SETTING

The Sonoma Foreland Basin of the western United States is a key archive of Early Triassic biotic dynamics (Figure 1). Bounded to the west by the Sonoma orogeny, it occupied a near-equatorial to mid-latitudinal position in open contact

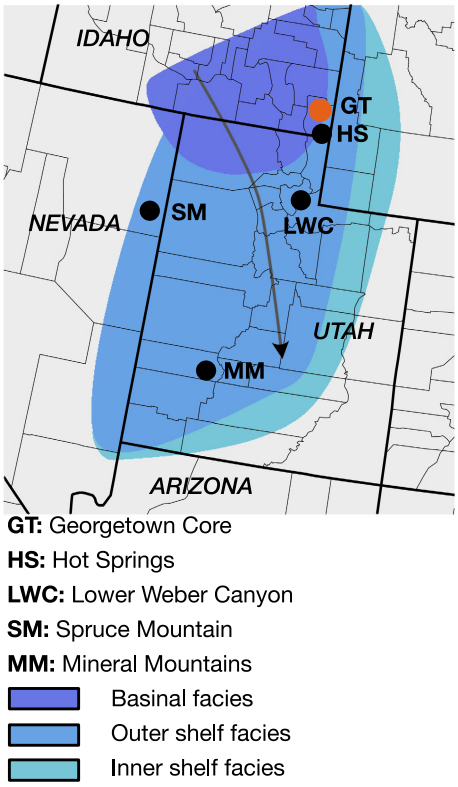

FIGURE 1 Early Triassic sedimentation in the Sonoma Foreland Basin, adapted from Brayard et al. (2013); arrow shows direction of the Smithian transgression and facies belts at the peak Smithian transgression, after Lucas et al. (2007), Brayard et al. (2013), Vennin et al. (2015). Key sections with geochemical records in the Sonoma Basin are marked: From north to south, these are the Georgetown core (Schneebeli-Hermann et al., 2020; this work), the Hot Springs section (Caravaca et al., 2017), the Spruce Mountain section (Saltzman & Sedlacek, 2013), the Lower Weber Canyon section (Grosjean et al., 2018; Decraene et al., 2023) and the Mineral Mountains section (Vennin et al., 2015; Thomazo et al., 2016, 2019). Note that the ?Spathian–?Anisian Moenkopi Platform of southern Utah, Nevada and California is not included.

with the eastern Panthalassic Ocean, forming a broad, shallow epicontinental basin traditionally subdivided into the northern and southern sub-basins (Caravaca et al., 2018). In eastern Idaho, the Lower Triassic is captured within three stratigraphic units (Kummel, 1943, 1954). The oldest, the Dinwoody Formation, consists of Griesbachian–Dienerian calcareous siltstones and limestones. It is overlain by Dienerian red to maroon calcareous siltstones of the Woodside Formation, which in turn is overlain by variably alternating shales and limestones of the Smithian–Spathian Thaynes Group (Kummel, 1943). Collectively, these lithostratigraphic units represent a mixed carbonate-siliciclastic succession, with considerable variations in the genesis, proportion and stoichiometry of carbonate mineralogy within and between lithostratigraphic units (Caravaca et al., 2017). Elsewhere in both the northern and southern subbasins, the Thaynes Group is described with different lithostratigraphic schemes and rests unconformably on Middle to Late Permian rocks with a major sedimentary hiatus corresponding to the Permian–Triassic transition and the Induan Stage (Goodspeed & Lucas, 2007; Lucas et al., 2007).

The Early Triassic Sonoma Basin palaeontological record is rich, including ammonoids (Brayard et al., 2013), conodonts (Solien, 1979), bivalves (Kummel, 1954), gastropods (Brayard et al., 2015), fish (Romano et al., 2017) and exceptionally diverse lagerstätte biota (Brayard et al., 2017; Smith et al., 2021). Despite the plenitude of palaeontological studies in the basin, only limited geochemical work has been conducted, particularly with regard to the Smithian–Spathian boundary (Figure 1). In the Spruce Mountain succession, Saltzman and Sedlacek (2013) identified a positive excursion in $\delta^{13}C_{carb}$ values, which was linked with the Smithian–Spathian boundary on the basis of radiogenic strontium isotope stratigraphy. In the Mineral Mountains, Thomazo et al. (2016) developed a multi-proxy $\delta^{13}C_{carb}$, $\delta^{13}C_{org}$, $\delta^{18}O$, $\delta^{34}S_{pyrite}$ and trace element record, which they used to conclude that the Smithian–Spathian carbon isotopic excursions recorded in the Thaynes Group resulted from a reduction of the sediment mixed layer and authigenic carbonate formation, rather than capturing secular evolution of the exogenic carbon cycle (see also Thomazo et al., 2019). In Lower Weber Canyon, Decraene et al. (2023) observed that $\delta^{34}S_{pyrite}$ and $\delta^{34}Fe_{pyrite}$ records likely reflect variations in the sedimentary and post-depositional environments, rather than capturing the global redox state of the ocean. Subsequent paired carbon isotopic studies ($\delta^{13}C_{carb}$-$\delta^{13}C_{org}$) in the Hot Springs section (Caravaca et al., 2017) captured the Smithian–Spathian carbon isotope variations recognised globally. However, while Caravaca et al. (2017) excluded significant diagenetic influence, they postulated that local environmental controls may have played an important role in modulating the observed $\delta^{13}C$ record.

The Georgetown core was recovered along the western bank of the Bear River in 2016 (42°28′41.0′′ N, 111°24′50.1′′ W), encompassing *ca* 150 m of ?Dienerian—Spathian stratigraphy (Figure 2; Schneebeli-Hermann et al., 2020). From bottom to top, it is composed of intercalated red siltstone and grey limestone beds attributed to the Dinwoody and Woodside formations (Unit I), thin alternations of laminated and bioturbated limestone of the Woodside Formation (Unit II), thickly laminated and bioclastic limestones of the *Meekoceras* Limestone (Thaynes Group; Unit III), argillaceous limestone of the Lower Shale (Thaynes Group; Unit IV) and palaeokarstified limestones of the Spathian *Tirolites* Limestone (Thaynes Group; Unit V) (all units after Schneebeli-Hermann et al., 2020). Previous work by Schneebeli-Hermann

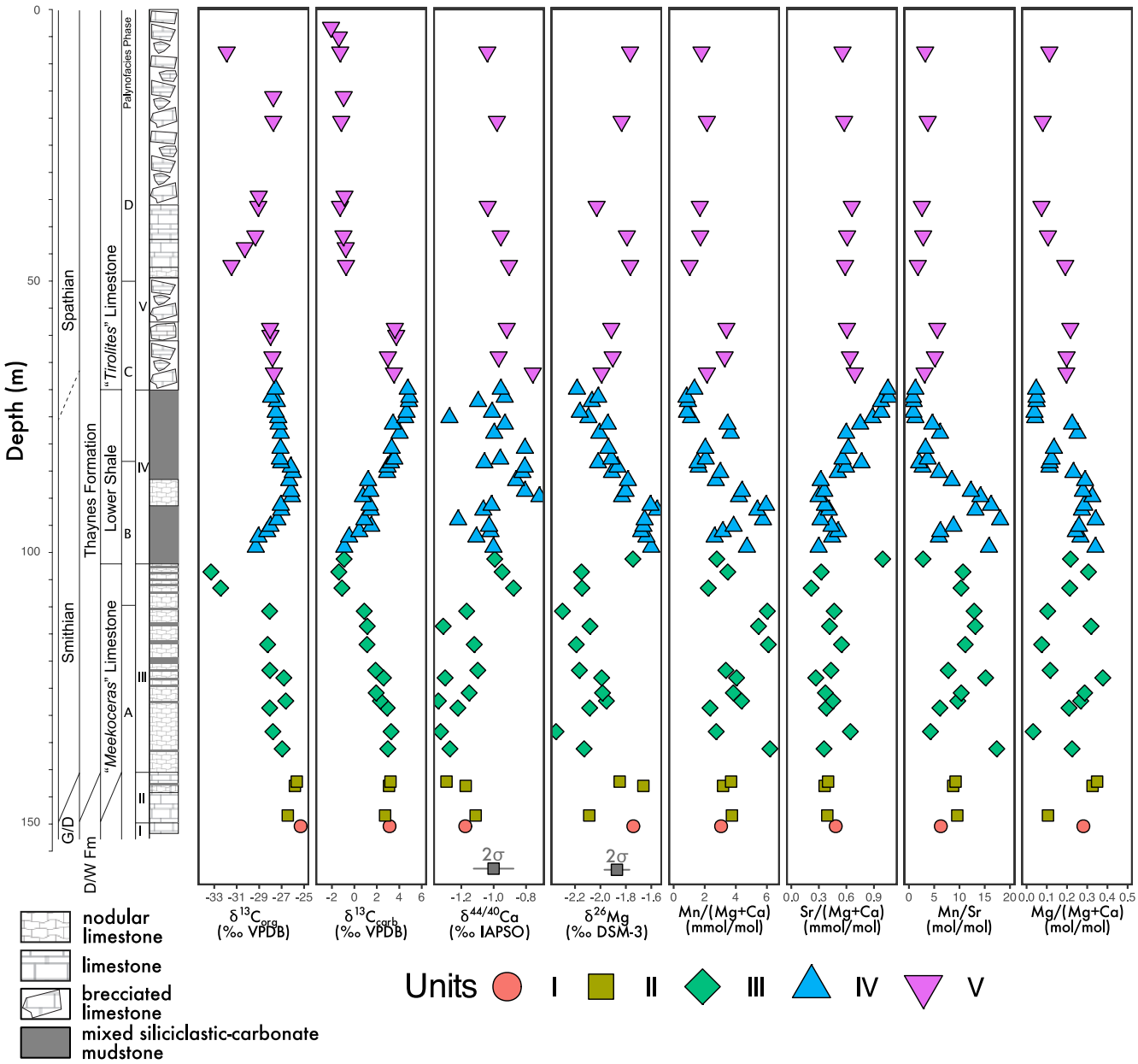

FIGURE 2 Stratigraphy and geochemistry of the Georgetown core. The stratigraphic section, lithostratigraphy, palynostratigraphy, chronostratigraphy, $\delta^{13}C_{carb}$, $\delta^{13}C_{org}$ and $\delta^{18}O$ data are adapted from Schneebeli-Hermann et al. (2020).

et al. (2020) established a robust palynological framework; reported rare, stratigraphically important conodonts and ammonoids; and presented a coupled $\delta^{13}C_{carb}$-$\delta^{13}C_{org}$ record. In combination, their study provides a coarse chronostratigraphic scaffold, with $\delta^{13}C_{carb}$ and $\delta^{13}C_{org}$ data interpreted as broadly reflecting global carbon cycle dynamics modulated to some extent by local bathymetry.

3 | METHODS

In this study, carbonate geochemical measurements were conducted on 47 powdered samples that were previously analysed for $\delta^{13}C_{org}$ values, $\delta^{13}C_{carb}$ values, $\delta^{18}O_{carb}$ values and palynology by Schneebeli-Hermann et al. (2020), spanning the extent of the Georgetown core. As summarised by Schneebeli-Hermann et al. (2020), samples were selected from bulk micrite and finely ground, avoiding diagenetic calcite veins, cracks, stylolites and large skeletal particles.

3.1 | Sample preparation

For each sample, 10 mg of bulk powdered sample was dissolved in 10 mL of a buffered 0.1 M acetic acid solution

in a 15mL centrifuge tube and allowed to react in an ultrasonicator for 4–8 h to ensure complete carbonate dissolution. It has been previously demonstrated that this protocol readily dissolves limestone and dolomites, but leaves less soluble sedimentary components, such as clays and iron-manganese oxides, largely unreacted (Husson et al., 2015). After dissolution, each sample was centrifuged, and the upper 3–8 mL of supernatant was pipetted into a fresh centrifuge tube. This supernatant formed the basis for the isotopic and elemental analyses detailed below.

3.2 | Ion chromatography

Dissolved sample aliquots were prepared, purified and collected for calcium and magnesium isotopic analyses via a Thermo/Dionex ICS-6000 ion chromatography (IC) system using a methanesulphonic acid eluent, following previously published methods (Razionale et al., 2022). Splits for calcium and magnesium were isolated from samples by collecting the eluent in timed windows. An in-line conductivity detector was used to quantify the mass of calcium or magnesium in each sample by calibrating the size of the calcium and magnesium peak areas with peaks produced by known calibration standards. Additionally, these peak areas were used to calculate molar Mg/(Mg + Ca) ratios. Once collected, samples were dried, treated with concentrated HNO_3 to oxidise and volatilise column-derived organic compounds, redried and dissolved at appropriate concentrations for isotopic analysis in 2% HNO_3.

3.3 | Major and trace element analysis

A suite of routine major element and trace element abundances were measured using a Thermo Scientific iCAP RQ inductively coupled plasma mass spectrometer (ICP-MS) at the University of Chicago. Kinetic energy discrimination (KED) mode was used to measure magnesium, calcium, manganese, iron, strontium and uranium abundances. In brief, small aliquots of the dissolved samples were subsampled, adjusted to approximately 10 ppm calcium in 2% HNO_3 prior to analysis, spiked with an appropriate internal standard solution containing scandium, yttrium and indium and quantified against a matrix-matched standard calibration curve. External reproducibility is estimated at 5–7% (1σ) for most elements, based upon replicate analysis of NIST reference materials RM-8301 (coral), RM-8301 (foraminifera) and an in-house carbonate standard. All data are reported as metal to calcium + magnesium ratios to standardise across samples with variable dolomite abundance.

3.4 | Multi-collector mass spectrometry: $\delta^{44/40}$Ca and δ^{26}Mg

All cation isotopic analyses were carried out using a Thermo Neptune XT multi-collector inductively coupled plasma mass spectrometer (MC-ICP-MS) at the University of Chicago. Calcium isotope analyses ($\delta^{44/40}$Ca) were performed using an ESI Apex-Ω desolvating nebuliser, which reduces hydride interferences to a considerable extent (Razionale et al., 2022). To avoid further interferences, a medium-resolution slit was used to avoid major polyatomic interferences, such as ArH_2^+, by maintaining a position on the low-mass shoulder. Sample-standard bracketing was used to correct for instrumental mass fractionation. Sample and standard solutions were diluted to the same concentration (*ca* 1 ppm calcium) to minimise concentration-dependent isotope effects, and known linear concentration-dependent effects within a 10% deviation from 1 ppm calcium were corrected using a concentration calibration. Strontium interferences were corrected by monitoring the double-charged $^{87}Sr^{2+}$ beam ($m/z = 43.5$). The ^{42}Ca, ^{43}Ca and ^{44}Ca beams were measured; after correction, $\delta^{44/40}$Ca values were calculated using established kinetic fractionation laws (Young et al., 2002), assuming no radiogenic ^{40}Ca excess. Triple-isotope plots ($\delta^{44/43}$Ca vs. $\delta^{44/42}$Ca) were used to ensure the mass dependence of strontium-corrected raw data prior to concentration correction. Data are reported relative to International Association for the Physical Sciences of the Oceans (IAPSO) sea water, and the long-term external reproducibility of this calcium isotope measurement protocol is ±0.12‰ (2σ) (Bryant et al., 2022; Razionale et al., 2022).

Magnesium isotope analyses (δ^{26}Mg) were introduced using a dual-path glass cyclonic chamber using a low-resolution slit and corrected for instrumental mass bias via sample-standard bracketing (Bryant et al., 2022). As with calcium, sample and standard solutions were diluted to the same concentration (*ca* 150 ppb magnesium) to minimise concentration-dependent isotope effects, although no concentration-dependent effect was observed during analytical runs. Triple-isotope plots ($\delta^{26/24}$Mg vs. $\delta^{26/25}$Mg) were used to ensure the mass dependence of raw data. Data are reported relative to Dead Sea Magnesium 3 (DSM-3), and the long-term external reproducibility of this magnesium isotope measurement protocol is ±0.10‰ (2σ).

3.5 | Gas source mass spectrometry: δ^{13}C and δ^{18}O

Most samples analysed in this study have existing $\delta^{13}C_{carb}$ and δ^{18}O data reported by Schneebeli-Hermann

et al. (2020), but $\delta^{13}C_{carb}$ and $\delta^{18}O$ measurements for samples ($n=4$) without reported isotopic data were conducted at the University of Chicago Stable Isotope Ratio Facility, using a GasBench II coupled to a Thermo-Finnigan Delta V Plus isotope ratio mass spectrometer in continuous-flow mode. Powdered samples (*ca* 150–200 μg of carbonate) were reacted with 103% phosphoric acid in helium-purged vials at 25°C. The evolved CO_2 gas was analysed against in-house tank CO_2 gas and calibrated against a suite of working in-house and external (NBS-18 and NBS-19) standards. Data for both $\delta^{13}C_{carb}$ and $\delta^{18}O$ are reported relative to V-PDB (Vienna-Pee Dee Belemnite), and the long-term external reproducibility for $\delta^{13}C$ is ±0.08‰ (2σ) and for $\delta^{18}O$ is ± 0.14‰ (2σ).

4 | RESULTS

The results of this study are presented stratigraphically in Figure 2. Following the framework of Schneebeli-Hermann et al. (2020), the core is subdivided into Unit I (?Dinwoody Formation), Unit II (?Woodside Formation), Unit III (*Meekoceras* Limestone), Unit IV (Lower Shale) and Unit V (*Tirolites* Limestone).

4.1 | Major, minor and trace elements

The Mg/(Mg + Ca) ratios range from 0.03 to 0.38 mol/mol (Figure 2), ranging between low-magnesium calcite [Mg/(Mg + Ca) < 0.04] and variable mixtures of dolomite and calcite [Mg/(Mg + Ca) > 0.04], although most samples have Mg/(Mg + Ca) > 0.04. In general, Mg/(Mg + Ca) ratios are the most variable in the lower part of the core, are high at the base of Unit IV before progressively declining upwards in the unit and remain relatively low in Unit V, especially in its uppermost portion.

Measured Mn/(Mg + Ca) and Sr/(Mg + Ca) ratios range from 1.0–8.0 and 0.19–1.0 mmol/mol, respectively (Figure 2). There is a significant positive correlation between Mn/(Mg + Ca) and Mg/(Mg + Ca) ratios ($R^2=0.32$, $p=3.8\times10^{-5}$; Figure 3A) and a significant negative correlation between Sr/(Mg + Ca) and Mg/(Mg + Ca) ratios ($R^2=0.50$, 3.5×10^{-8}; Figure 3B), both of which are particularly clear in Units IV and V. Stratigraphically, Mn/(Mg + Ca) ratios are high and variable in Units I–III, progressively decline through Unit IV and remain low and relatively stable in Unit V (Figure 2). Correspondingly, Sr/(Mg + Ca) ratios are quite low in Units I–III, before sharply increasing in the middle of Unit IV to approximately 1.0 mmol/mol (Figure 2). Above, Sr/(Mg + Ca) ratios remain relatively stable at *ca* 0.6 mmol/mol throughout Unit V. The Mn/Sr ratios broadly parallel Mn/(Mg + Ca) ratios:

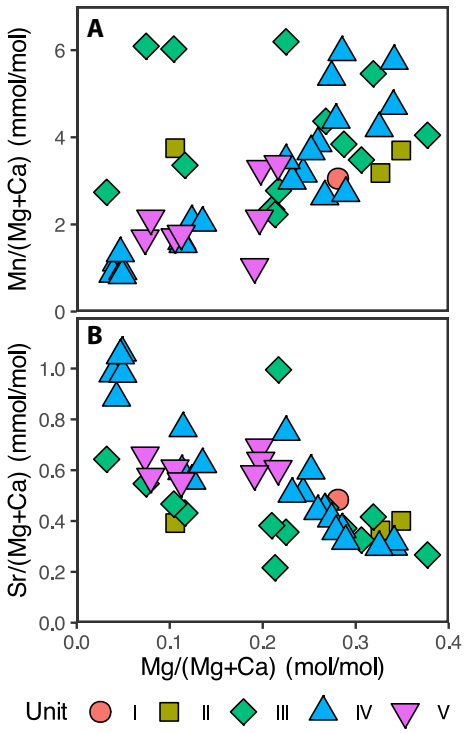

FIGURE 3 Co-variation of trace-metal ratios with Mg/(Mg + Ca) ratios in the Georgetown core. (A) Mn/(Mg + Ca) ratios versus Mg/(Mg + Ca) ratios ($R^2=0.32$, $p=3.8\times10^{-5}$); (B) Sr/(Mg + Ca) ratios versus Mg/(Mg + Ca) ratios ($R^2=0.50$, $p=3.5\times10^{-8}$).

They are comparatively elevated (average = 10 mol/mol) and variable in Units I–III, progressively decrease through Unit IV and remain comparatively low (average = 3.5 mol/mol) and stable in Unit V (Figure 2).

4.2 | Magnesium isotopes

Measured $\delta^{26}Mg$ values range from −2.35 to −1.55‰, with an average value of −1.93‰ relative to DSM-3. In general, $\delta^{26}Mg$ values broadly capture a significant positive correlation when plotted against Mg/(Mg + Ca) ratios ($R^2=0.30$, $p=7.6\times10^{-5}$): This is especially apparent in Unit IV and to a lesser extent in Units I–II (Figure 4A). Stratigraphically, $\delta^{26}Mg$ values are comparatively variable in Units I–II, low and stable in Unit III (average = −2.1‰), reach a maximum at the base of Unit IV before progressively declining through the unit and stabilise in Unit V (average = −1.9‰) (Figure 2).

4.3 | Calcium isotopes

In a similar vein, measured $\delta^{44/40}Ca$ values range from −1.34 to −0.72‰, with an average value of −1.04‰.

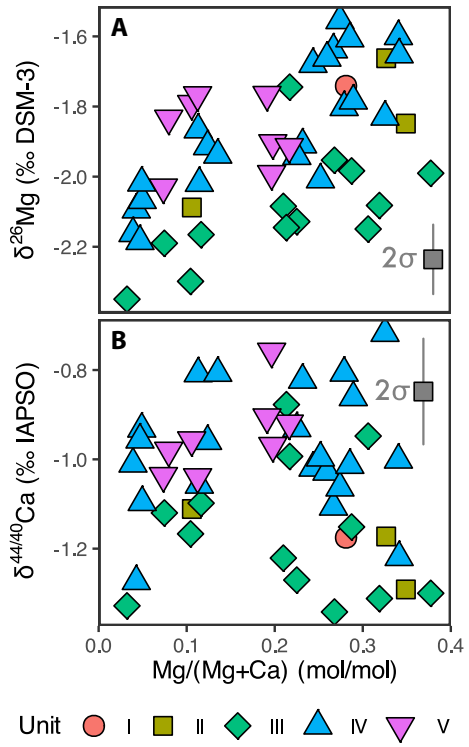

FIGURE 4 Co-variation of cation isotope ratios with Mg/(Mg + Ca) ratios in the Georgetown core. (A) δ^{26}Mg values versus Mg/(Mg + Ca) ratios ($R^2 = 0.30$, $p = 7.6 \times 10^{-5}$); (B) $\delta^{44/40}$Ca values versus Mg/(Mg + Ca) ratios ($R^2 = 0.01$, $p = 0.55$).

Stratigraphically, $\delta^{44/40}$Ca values are relatively low (average = −1.22‰) and stable until the top of Unit III, where they sharply increase at 107.5 m to −0.88‰ (Figure 2). Above, $\delta^{44/40}$Ca values decline until the middle of Unit IV (90.5 m), where they again sharply increase to −0.72‰. There, $\delta^{44/40}$Ca values decline above to the topmost portion of Unit IV (72.05 m), where they stabilise at approximately −0.95‰. Unlike the geochemical properties above, there is no strong connection between $\delta^{44/40}$Ca values and Mg/(Mg + Ca) ratios ($R^2 = 0.01$, $p = 0.55$; Figure 4B), or between $\delta^{44/40}$Ca and δ^{26}Mg values ($R^2 = 0.05$, $p = 0.14$). However, in Unit IV, there is a substantial negative correlation between $\delta^{44/40}$Ca and Sr/(Mg + Ca), especially above 90.5 m ($R^2 = 0.43$, $p = 8.6 \times 10^{-3}$).

4.4 | Comparison of δ^{26}Mg, $\delta^{44/40}$Ca and trace–metal ratios with existing records

Existing $\delta^{13}C_{carb}$ and $\delta^{13}C_{org}$ records for the Georgetown core (see Schneebeli-Hermann et al., 2020) are broadly similar to each other, although differences in their expression emerge in the upper portion of the recovered core (Figure 2). Relatively invariant $\delta^{13}C_{carb}$ and $\delta^{13}C_{org}$ values are recorded in Units I–III, followed by a sharp decrease in both records near the top of Unit III. In Unit IV, $\delta^{13}C_{carb}$ values progressively increase from a nadir of −0.9‰ at the base of Unit IV to 4.9‰ at the top of Unit IV; in contrast, while $\delta^{13}C_{org}$ values also increase from the base of Unit IV, they peak at 86.0 m and remain stable throughout the rest of Unit IV. In Unit V, $\delta^{13}C_{carb}$ values dramatically drop 20 m above the base of the unit (at 47.5 m) to −0.8‰ and slightly decline upwards to the top of the core. However, $\delta^{13}C_{org}$ values are highly variable in Unit V, decreasing to −31.5‰ before rising to −27.7‰ and again falling to −31.9‰ at the top of the measured core.

Sample $\delta^{13}C_{carb}$ values show correlations with several of the geochemical proxies measured here, although the exact nature of those relationships is not consistent throughout the Georgetown core and, instead, are piecewise correlated within individual lithostratigraphic units. In Units I–III, there exists a clear negative correlation between $\delta^{13}C_{carb}$ and $\delta^{44/40}$Ca values ($R^2 = 0.62$, $p = 1.8 \times 10^{-4}$; Figure 5B), although there is no clear correlation with the extent of dolomitisation (i.e. Mg/(Mg + Ca) ratios; $R^2 = 0.00$, $p = 0.93$; Figure 5A). Above, in Unit IV, there are significant negative correlations between $\delta^{13}C_{carb}$ and δ^{26}Mg values ($R^2 = 0.81$, $p = 1.0 \times 10^{-8}$; Figure 5C), Mg/(Mg + Ca) ratios ($R^2 = 0.75$, $p = 1.9 \times 10^{-7}$; Figure 5A), Mn/(Mg + Ca) ratios ($R^2 = 0.51$, $p = 1.8 \times 10^{-4}$) and Mn/Sr ratios ($R^2 = 0.71$, $p = 1.9 \times 10^{-5}$; Figure 6A), along with a significant positive correlation between $\delta^{13}C_{carb}$ values and Sr/(Mg + Ca) ratios ($R^2 = 0.77$, $p = 8.8 \times 10^{-8}$). Finally, in Unit V, there is a significant positive correlation between $\delta^{13}C_{carb}$ values and Mn/(Mg + Ca) ratios ($R^2 = 0.59$, $p = 0.025$).

5 | DISCUSSION

Below, the geochemical behaviour of the Georgetown core is linked with lithologic variations, enabling an investigation of the extent to which local and/or post-depositional factors may have influenced the carbonate geochemistry of the Georgetown core. Based on the absence of co-variation between $\delta^{13}C_{carb}$ and δ^{18}O values in the Georgetown core, Schneebeli-Hermann et al. (2020) concluded that the $\delta^{13}C_{carb}$ values in the Georgetown core were not overprinted by diagenesis, and instead reflect the evolution of global oceanic DIC. While co-variation between $\delta^{13}C_{carb}$ and δ^{18}O values may be indicative of certain diagenetic mechanisms, such as meteoric or late-burial diagenesis, co-variation is not necessarily expected in other diagenetic settings (Swart, 2015), and so this absence of covariation does not necessarily exclude the possibility of extensive post-depositional alteration. Moreover, carbonate δ^{18}O values are particularly prone to diagenetic resetting throughout their entire post-depositional trajectory, especially compared to $\delta^{13}C_{carb}$ values (Banner & Hanson, 1990;

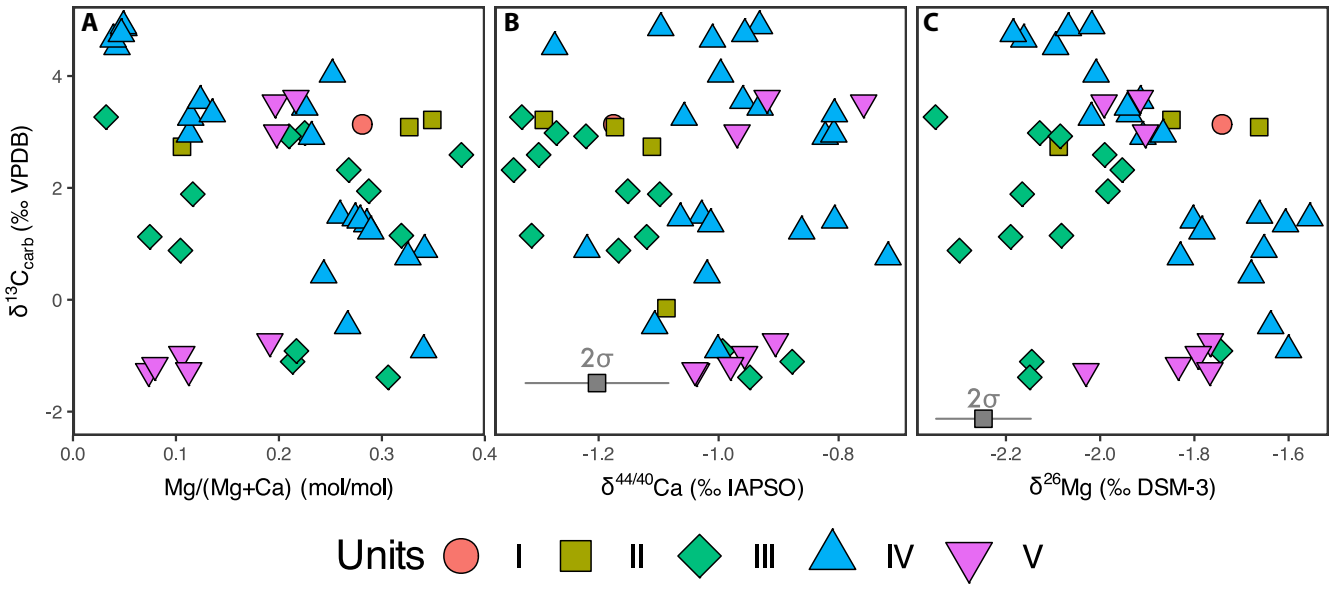

FIGURE 5 Co-variation of $\delta^{13}C_{carb}$ values with trace-metal and isotopic ratios in the Georgetown core. (A) $\delta^{13}C_{carb}$ values vs. Mg/(Mg + Ca) ratios ($R^2 = 0.06$, $p = 0.10$); (B) $\delta^{13}C_{carb}$ values versus $\delta^{44/40}Ca$ values ($R^2 = 0.02$, $p = 0.39$; for Units I-III, $R^2 = 0.62$, $p = 1.8 \times 10^{-4}$) (C) $\delta^{13}C_{carb}$ values versus $\delta^{26}Mg$ values ($R^2 = 0.10$, $p = 0.02$).

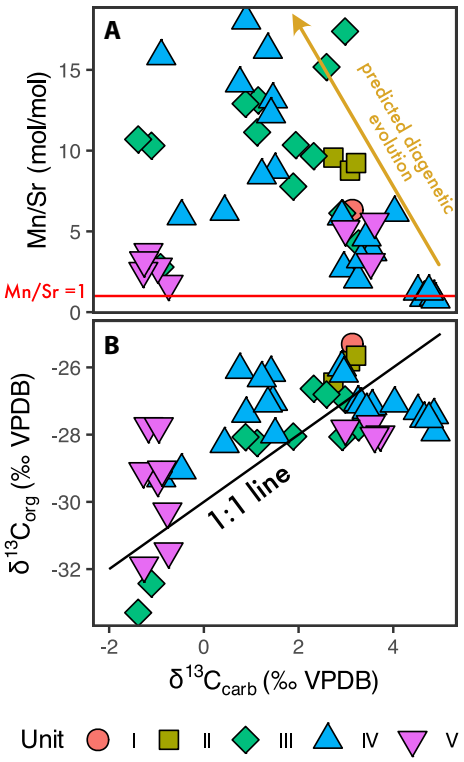

FIGURE 6 Traditional indices of diagenesis: (A) Mn/Sr ratios versus $\delta^{13}C_{carb}$ values and (B) $\delta^{13}C_{org}$ values versus $\delta^{13}C_{carb}$ values in the Georgetown core. The red line on (A) marks Mn/Sr = 1 mol/mol, which often serves as a 'threshold value' to detect extensive post-depositional alteration (Derry et al., 1992). The black line on (B) is a 1:1 line, with $\delta^{13}C_{org}$ values offset by $\varepsilon = 30‰$ relative to $\delta^{13}C_{carb}$ values.

Ahm et al., 2018). Therefore, even if $\delta^{13}C_{carb}$ and $\delta^{18}O$ values developed a co-variation during early diagenetic stages (e.g., meteoric diagenesis), $\delta^{18}O$ values may have been subsequently reset during later post-depositional stages, disrupting any existing correlation. To this end, additional geochemical proxies are explored that suggest other diagenetic mechanisms may have been significant in the Georgetown core.

5.1 | Geochemical evidence for diagenetic alteration

5.1.1 | Manganese/strontium ratios

Manganese-to-strontium ratios (Mn/Sr) have often been used as a diagenetic tracer within the geological record (Derry, 2010), since Mn/Sr ratios in modern sea water are very low while those in diagenetic fluids can be significantly higher (Derry et al., 1992). In general, manganese is more soluble under anoxic conditions, due to the dramatic difference in solubility between the reduced Mn(II) and oxidised Mn(IV) species (Tebo, 1991). Elevated manganese concentrations in pore fluids are thus often associated with anoxia and organic carbon remineralisation—which, in turn, can lower $\delta^{13}C_{carb}$ values of carbonate minerals recrystallised under such conditions, leading to a negative correlation between Mn/Sr ratios and $\delta^{13}C_{carb}$ values (Brand & Veizer, 1980; Klinkhammer, 1980). In contrast, strontium tends to decrease in diagenetically stabilised

carbonates because (i) the strontium partition coefficient is larger in aragonite and biogenic calcite (K_D = 0.2–1.1) than in low-magnesium calcite (K_D = 0.03–0.1) or dolomite (K_D = 0.02–0.06), and aragonite undergoes alteration to low-magnesium calcite or dolomite during diagenetic stabilisation (Banner & Hanson, 1990; Banner, 1995; Zhang & DePaolo, 2020), and (ii) there is a strong kinetic dependence for strontium incorporation into carbonates, and the rate of primary carbonate precipitation is more rapid than the rate of diagenetic recrystallisation (Tang et al., 2008b; DePaolo, 2011).

In the Georgetown core, the clear negative co-variation between Mn/Sr ratios and $\delta^{13}C_{carb}$ values in Units I–IV suggests that the $\delta^{13}C_{carb}$ values were influenced by an anoxic diagenetic fluid whose elemental composition varied significantly from sea water (Figure 6A). Diagenetic recrystallisation under anoxic conditions was most important in Units I–III and became progressively less influential throughout Unit IV, throughout which Mn/Sr ratios decrease. Independent evidence for anoxic pore water conditions during the deposition and diagenetic stabilisation of the Lower Shale comes from its laminar, non-bioturbated sedimentary fabrics (Schneebeli-Hermann et al., 2020). Therefore, any systematic changes in carbonate redox proxies throughout this interval should be interpreted through the lens of an anoxic diagenetic environment, and so are likely not directly related to secular Earth system evolution. Most samples lie well above the often-cited Mn/Sr threshold value of 1 mol/mol above which diagenesis is traditionally interpreted to have influenced carbonate geochemistry (Derry et al., 1992) (although note that lower Mn/Sr ratios do not inherently exclude certain diagenetic styles, especially in carbonate platforms; see Swart et al., 2014; Higgins et al., 2018).

5.1.2 | Dolomitisation

The presence of extensive—if incomplete—dolomitisation in the Georgetown core additionally suggests that diagenetic processes were influential in shaping the carbonate geochemistry of the Georgetown core. While replacive dolomitisation inherently entails a major reset of the major cation carbonate geochemistry, this process does not necessarily translate to dramatic changes in associated trace-metal and $\delta^{13}C_{carb}$ signatures (Mueller et al., 2020). Under conditions with lower water:rock ratios, where the availability of magnesium ions may be the limiting factor for dolomitisation, $\delta^{13}C$ ratios in a dolomite may reflect the influence of the precursor carbonate mineral (more 'sediment-buffered dolomitisation'). On the other end of the spectrum with very high water:rock ratios, dolomites may instead capture the $\delta^{13}C$ value of largely unevolved regional sea water DIC ('fluid-buffered dolomitisation') (Blättler et al., 2015; Higgins et al., 2018; Ahm et al., 2021). These different modes have distinct implications for the genesis of $\delta^{13}C_{carb}$ signatures. More sediment-buffered dolomites tend to preserve original, or early diagenetic, $\delta^{13}C_{carb}$ values that can be decoupled from secular sea water DIC evolution, whereas in fluid-buffered dolomites the exchange of carbon between the original sediment and the diagenetic fluids is generally sufficient enough to reset associated $\delta^{13}C_{carb}$ values towards the diagenetic fluid—which is often, but not always, unevolved sea water DIC (Bold et al., 2020; Crockford et al., 2020; Nelson et al., 2021).

In the Georgetown core, strong correlations between the extent of dolomitisation [Mg/(Mg + Ca) ratios] and trace-metal, $\delta^{26}Mg$ and $\delta^{13}C_{carb}$ values (Figures 3, 4A and 5B), collectively suggest that the dolomitic fraction captures a geochemical signature that is distinct from the calcitic fraction. These co-variations are especially prominent in Unit IV and coincide with the largest excursion in $\delta^{13}C_{carb}$ values observed in the Georgetown core, suggesting that the geochemical record of this interval may be modulated more so by mineralogical variations than secular palaeoceanographic change. In particular, the positive association with Mn/(Mg + Ca) ratios (Figure 3A), and the negative association with $\delta^{13}C_{carb}$ values (Figure 5A), suggests that the dolomitisation process was anoxic and associated with organic carbon remineralisation in a relatively closed system. This process, in turn, would lead to increased pore water manganese concentrations and decreased local DIC $\delta^{13}C$ values and is quantitatively explored below in Section 5.2.2.

5.1.3 | Calcium and magnesium isotope ratios

Early marine diagenesis in carbonate rocks can be difficult to identify petrographically or with traditional geochemical indicators, although it is capable of altering even the most resistant chemical and isotopic signatures (Shinn et al., 1983; Higgins et al., 2018; Ahm et al., 2021). The calcium and magnesium isotope systems can be sensitive to this process and help determine the extent to which carbonate geochemistry is controlled by the original sediment chemistry (reflecting 'sediment-buffered' conditions) or the diagenetic fluid chemistry ('fluid-buffered' conditions). Fluid- and sediment-buffered are defined with respect to a particular elemental or isotopic system, due to mass balance considerations: for instance, a sample can be fluid-buffered with respect to $\delta^{18}O$ while being sediment-buffered with respect to $\delta^{13}C_{carb}$ due to

the different concentrations of oxygen and carbon for the original sediment and diagenetic fluid. In general, the range of sediment-buffered to fluid-buffered conditions has been defined with respect to $\delta^{13}C_{carb}$ (Ahm et al., 2018). In this context, calcium isotope ratios serve as an effective tracer for the extent of early marine diagenesis, with $\delta^{44/40}Ca$ values increasing as diagenetic alteration transitions from more sediment-buffered to more fluid-buffered. This relationship emerges because $\delta^{44/40}Ca$ values of primary carbonates are largely dictated by mineralogical and kinetic controls (Tang et al., 2008a; DePaolo, 2011), whereas the diagenetic environment promotes reactions close to equilibrium, and the equilibrium fractionation (α) between carbonates and diagenetic fluid is approximately 1 (Fantle & DePaolo, 2007; Jacobson & Holmden, 2008). Since sea water $\delta^{44/40}Ca$ values are invariably higher than marine carbonate $\delta^{44/40}Ca$ values, and the diagenetic fluid during early marine diagenesis is derived from sea water, sedimentary $\delta^{44/40}Ca$ values should increase as early marine diagenesis progresses. The magnitude of diagenetic $\delta^{44/40}Ca$ change is usually significantly larger than what can be produced by perturbations to the global marine calcium reservoir such as from increased weathering rates and/or ocean acidification (Komar & Zeebe, 2011, 2016), as results from fully coupled calcium and carbon cycle models show that carbonate compensation effectively stabilises calcium concentrations in response to such perturbations, limiting global marine $\delta^{44/40}Ca$ excursions to an effective maximum of *ca* 0.3‰ in response to forcing events.

In turn, coupled $\delta^{44/40}Ca$ and $\delta^{26}Mg$ ratios are useful for examining dolomitisation styles. Open system, fluid-buffered marine dolomites (see Section 5.1.2) have $\delta^{26}Mg$ values that are approximately 2‰ lighter than contemporaneous sea water and $\delta^{44/40}Ca$ values that approach contemporaneous sea water (Ahm et al., 2018; Higgins et al., 2018). Where magnesium supply is limiting, more sediment-buffered dolomites have $\delta^{26}Mg$ values that can be variably heavier than fluid-buffered dolomites due to Rayleigh distillation of the magnesium during dolomitisation and $\delta^{44/40}Ca$ values that can be inherited from the precursor carbonate (Blättler et al., 2015). Anti-correlation between $\delta^{44/40}Ca$ and $\delta^{26}Mg$ values can therefore signal variably open-/closed-system pore fluid behaviour, which directly impacts magnesium supply; for example, these conditions could occur if diffusion is the limiting factor for authigenic dolomite formation (Blättler et al., 2015). This anti-correlation can be associated with negative $\delta^{13}C_{carb}$ values if dolomite formation is associated with bacterial sulphate reduction. Together, these patterns may enable us to test the hypothesis of Thomazo et al. (2016) that the expression of the Smithian–Spathian boundary excursion in the Thaynes Group is due to widespread authigenic carbonate precipitation in the boundary interval.

In the Georgetown Core, there is a clear negative co-variation between $\delta^{13}C_{carb}$ and $\delta^{44/40}Ca$ values in Units I–III, which is interpreted as reflecting a shift from sediment-buffered to fluid-buffered diagenesis as the major control of $\delta^{13}C_{carb}$ values in the lower part of the core (Figure 5B). Samples with relatively high proportions of dolomite have relatively light $\delta^{44/40}Ca$ and relatively heavy $\delta^{26}Mg$ values compared to what would be anticipated from fluid-buffered dolomitisation, given estimates of Triassic sea water $\delta^{44/40}Ca$ and $\delta^{26}Mg$ (about −0.2 and 0.3‰, respectively; Farkaš et al., 2007; Li et al., 2015), supporting previous interpretations that the dolomitisation in the Georgetown core is comparatively sediment-buffered (see Section 5.2.2 for further discussion). However, the absence of a strong negative co-variation between $\delta^{44/40}Ca$ and $\delta^{26}Mg$ values suggests that authigenic dolomite precipitation under anaerobic conditions (e.g., bacterial sulphate reduction, methanogenesis) was not a major contributor to the carbonate budget of the Georgetown core.

5.1.4 | Paired $\delta^{13}C_{carb}$ and $\delta^{13}C_{org}$ analyses

Paired $\delta^{13}C_{carb}$ and $\delta^{13}C_{org}$ records of the Georgetown core (Figure 6B) also suggest that diagenetic processes shaped the carbonate geochemical record of the Georgetown core. In principle, these two measurements ought to co-vary if both records are primary and there are no significant changes in the isotopic fractionation between DIC and organic matter within the studied interval and region (see Knoll et al., 1986; Oehlert & Swart, 2014). While $\delta^{13}C_{carb}$ and $\delta^{13}C_{org}$ records broadly co-vary in Units I–III, $\delta^{13}C_{org}$ values are largely stable in Unit IV despite a considerable range in $\delta^{13}C_{carb}$ (Figure 6B). The reverse is true in Unit V, where $\delta^{13}C_{carb}$ values largely do not change despite considerable variation in $\delta^{13}C_{org}$ values. Noting this, Schneebeli-Hermann et al. (2020) argued that the $\delta^{13}C_{org}$ record may have been influenced by changes in the constitution of organic matter, paralleling changes in regional eustasy and local depositional environment, and so to some extent captured changes in the isotopic fractionation between DIC and organic matter rather than the evolution of regional DIC. While there is certainly some evidence for changing organic matter composition (see Schneebeli-Hermann et al., 2020), another, non-mutually exclusive cause of this relationship may be that the $\delta^{13}C_{carb}$ record is influenced by post-depositional alteration, due to the extensive co-variation between $\delta^{13}C_{carb}$ values and carbonate diagenetic tracers, as discussed above.

5.2 | Lithostratigraphic variation in diagenetic style

As outlined above, the carbonate geochemical record of the Georgetown core was mediated to some degree by post-depositional processes, although patterns of diagenesis are not uniform in either style or extent throughout the Georgetown core. Below, the different diagenetic modes and processes that predominated throughout the core are outlined on a lithostratigraphic unit-by-unit basis, and linked to the sedimentological evolution of the Georgetown core.

5.2.1 | Units I–III: Dinwoody Formation, Woodside Formation and Meekoceras Limestone

The lower Georgetown core generally reflects early marine diagenetic behaviour, rather than global $\delta^{13}C_{carb}$ evolution, based on the clear co-variation between $\delta^{13}C_{carb}$ and $\delta^{44/40}Ca$ values (Figure 5B). In an early marine diagenetic framework, the decline in $\delta^{13}C_{carb}$ values linked with a concurrent positive shift in $\delta^{44/40}Ca$ values captures a modest transition from more sediment-buffered conditions at the base of the core towards more fluid-buffered conditions towards the top of Unit III (Figure 2). Additionally, the *Meekoceras* Limestone is largely composed of nodular limestones, which have been proposed to form via the early diagenetic dissolution of aragonite and subsequent re-precipitation of calcite (Jenkyns, 1975; Kennedy & Garrison, 1975). Diagenetic stabilisation in the lower Georgetown core likely occurred under predominantly anoxic conditions in both the sediment-buffered and fluid-buffered endmembers, given that elevated Mn/(Mg + Ca) ratios are observed throughout the lower Georgetown core (Figure 2), and that the formation of nodular carbonates is commonly promoted by anoxic conditions (Jenkyns, 1975; Kennedy & Garrison, 1975).

In general, Units I–III capture a gradual transition from the more siliciclastic Woodside and Dinwoody formations to the limestone-dominated *Meekoceras* Limestone (Figure 2). This change from siliciclastic to carbonate-dominated facies is associated with a shift from closed-system to open-system diagenetic behaviour, in which the siliciclastic layers preferentially restricted early-diagenetic fluid migration in Units I–II, similar to the mechanism proposed by Nelson et al. (2021) to explain Cryogenian $\delta^{13}C_{carb}$ variability in the Panamint Range. Furthermore, as $\delta^{13}C_{carb}$ values are stable in the sediment-buffered interval (*ca* 3‰; 155–125 m), this value is interpreted as capturing the $\delta^{13}C$ value of local DIC, modified by the fractionation associated with carbonate precipitation. The subsequent decrease in $\delta^{13}C_{carb}$ values is largely attributed to early marine diagenesis, possibly driving carbonate geochemistry towards the carbon isotopic composition of an evolved, anoxic diagenetic fluid.

5.2.2 | Unit IV: Lower Shale

In the Georgetown core, the carbonate geochemical record of the Lower Shale is pervasively affected by dolomitisation, with no clear co-variation between co-occurring $\delta^{44/40}Ca$ and $\delta^{26}Mg$ values. The extent of dolomitisation is greatest at the base of Unit IV and progressively decreases throughout the unit. Furthermore, the sharp negative co-variation between $\delta^{13}C_{carb}$ values and $\delta^{26}Mg$ values, Mg/(Mg + Ca) ratios and Mn/(Mg + Ca) ratios in the Lower Shale suggests that $\delta^{13}C_{carb}$ values were strongly influenced by the dolomitisation process. Therefore, the geochemical record of the Lower Shale is interpreted as heavily influenced by relatively sediment-buffered anoxic dolomitisation, with the extent of dolomitisation decreasing from the base to the top of the unit.

To examine how partial dolomitisation may have influenced the geochemistry of the Lower Shale, a simple model—assuming that the Mg/(Mg + Ca) ratios reflect linear mixing between calcite and dolomite fractions—was constructed, from which mixing trends were calculated for $\delta^{13}C_{carb}$, $\delta^{26}Mg$, Sr/(Mg + Ca) and Mn/(Mg + Ca) values (Figure 7). There was no attempt to model $\delta^{44/40}Ca$ values: given the interpretation of the dolomite as partially 'sediment-buffered', the $\delta^{44/40}Ca$ values of the dolomitic fraction may be partially and/or variably retained from the precursor carbonate mineral (Blättler et al., 2015; Nelson et al., 2021), and the implications of the $\delta^{44/40}Ca$ record are explored below. The $\delta^{13}C_{carb}$, Sr/(Mg + Ca) and Mn/(Mg + Ca) values for endmember calcite [Mg/(Mg + Ca) = 0.03] and dolomite [Mg/(Mg + Ca) = 0.50] were determined using an orthogonal linear regression between the respective geochemical parameters and Mg/(Mg + Ca) ratios through all data points in Unit IV. Since Mg/(Ca + Mg) ratios are stoichiometrically dominated by the dolomitic fraction, endmember $\delta^{26}Mg$ values were determined using a orthogonal linear regression between observed $\delta^{26}Mg$ values and 1/[Mg/(Mg + Ca)] ratios. These regressions yield a calcite endmember with $\delta^{13}C_{carb} = 5.3‰$, $\delta^{26}Mg = -2.3‰$, Sr/(Mg + Ca) = 1.00 mmol/mol and Mn/(Mg + Ca) = 0.3 mmol/mol. In turn, the dolomite endmember would have $\delta^{13}C_{carb} = -2.2‰$, $\delta^{26}Mg = -1.6‰$, Sr/(Mg + Ca) = 0.01 mmol/mol and Mn/(Mg + Ca) = 7.1 mmol/mol. As a consistency check, these modelled isotopic values are compared to independent constraints on Triassic sea water compositions.

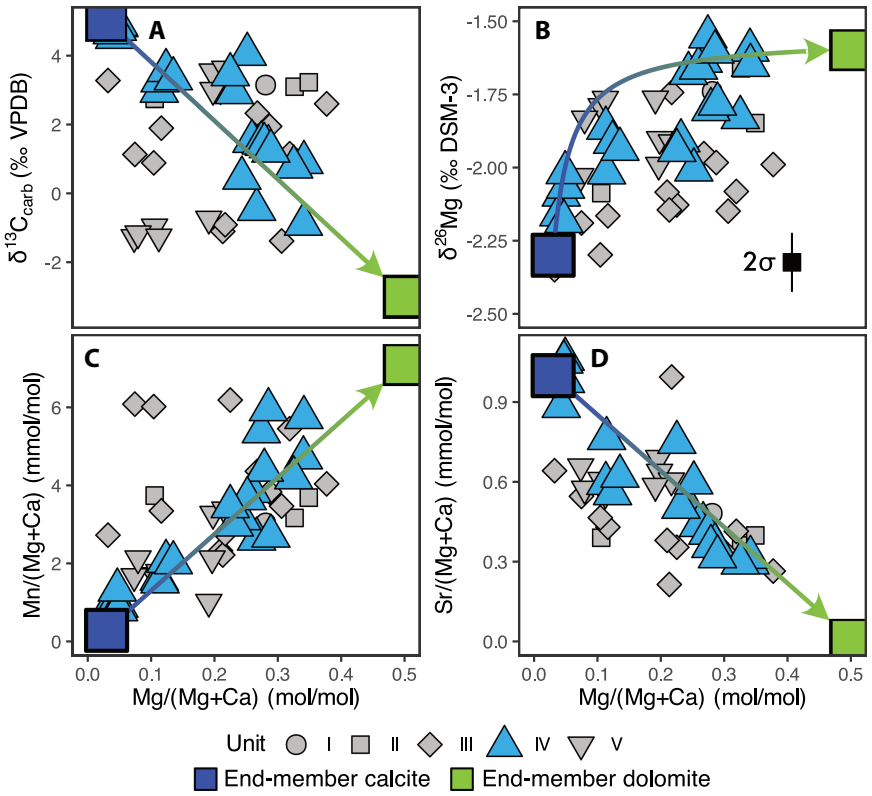

FIGURE 7 Mixing model of a modelled primary calcite endmember with a modelled secondary dolomite endmember as described in the text, compared to Georgetown core observations (Unit IV highlighted). (A) $\delta^{13}C_{carb}$ values versus Mg/(Mg + Ca) ratios; (B) $\delta^{26}Mg$ values versus Mg/(Mg + Ca) ratios; (C) Mn/(Mg + Ca) ratios versus Mg/(Mg + Ca) ratios; (D) Sr/(Mg + Ca) ratios versus Mg/(Mg + Ca) ratios.

Magnesium

The dolomite endmember $\delta^{26}Mg$ value (−1.6‰) is slightly heavier than would be predicted based on Triassic sea water $\delta^{26}Mg$ estimates (approximately 0.0–0.3‰) derived from existing Triassic dolomite (Geske et al., 2012; Li et al., 2015; Hu et al., 2017, 2021) and fluid-inclusion (Xia et al., 2020, 2024) $\delta^{26}Mg$ data. Under ambient marine conditions, the fractionation factor between sea water and dolomite is $\alpha = 0.998$, leading to a 2.0‰ offset between sea water and fully fluid-buffered dolomites (Higgins & Schrag, 2010; Li et al., 2015). Given this discrepancy, the $\delta^{26}Mg$ value of the dolomite endmember is interpreted as driven by limited Rayleigh distillation of magnesium during dolomitisation. The modelled endmember value represents the furthest progression of magnesium distillation within the Georgetown Core. Several samples have $\delta^{26}Mg$ values that lie beneath the mixing curve in Figure 7B, which are interpreted as reflecting dolomitisation from fluids that had experienced less Rayleigh distillation with respect to magnesium. Furthermore, given the near-linear decrease in $\delta^{26}Mg$ values throughout Unit IV (Figure 2), the progression of Rayleigh distillation in the dolomitising fluids is proposed to decrease up-section, resulting in the observed discrepancy between the mixing model and the observed data. In contrast, the calcite endmember $\delta^{26}Mg$ value (−2.3‰) aligns well with predictions for calcite precipitated from estimated Triassic sea water $\delta^{26}Mg$. While modern carbonate sediment $\delta^{26}Mg$ values occupy a fairly broad range (−5.5 to −1.5‰, with considerable mineralogical dependence), the average offset between ambient sea water and modern carbonates ($\Delta = -2.2$‰) is broadly comparable to the observed offset between the modelled calcite endmember and estimates of Triassic sea water (Saenger & Wang, 2014; Higgins et al., 2018).

A similar mixing model was used to explain the observed $\delta^{26}Mg$ record of the Middle Triassic Geshan section, and derived near-identical values for $\delta^{26}Mg_{calcite}$ and $\delta^{26}Mg_{dolomite}$, supporting prior estimates of Triassic sea water composition and suggesting that dolomitisation from sea water-derived fluids in a partially magnesium-limited setting may be relatively common (Hu et al., 2017). Furthermore, several prior studies have observed anomalously heavy $\delta^{26}Mg$ records from dolomitic Early Triassic successions, which have been attributed to local basin and/or pore-water restriction with respect to magnesium concentrations (Geske et al., 2012; Hu et al., 2021).

Carbon

The modelled calcite $\delta^{13}C_{carb}$ value lies within the range of estimated Smithian–Spathian sea water DIC based on well-preserved articulate brachiopods (Korte et al., 2005), but the modelled dolomite $\delta^{13}C_{carb}$ value lies well below this range. This phenomenon can be readily explained by the remineralisation of sedimentary organic matter, lowering $\delta^{13}C_{DIC}$ values of the dolomitising fluid. Any dolomitisation occurring within these fluids would have reduced $\delta^{13}C_{carb}$ values, while $\delta^{13}C_{org}$ values would be unaffected, as observed in the Lower Shale. This mechanism

would be supported under increasingly anoxic conditions, which would imply more closed-system behaviour and the retention of organic-matter derived DIC—the same conditions that would lead to elevated pore water manganese concentrations and elevated Mn/(Mg + Ca) ratios in dolomite (Derry, 2010). The end-member calcite $\delta^{13}C_{carb}$ value (5‰) may also be a suitable record of regional DIC $\delta^{13}C$ values during the deposition of Unit IV, especially near the contact of the Lower Shale and the *Tirolites* Limestone.

Calcium

The mixing model proposed here does not adequately explain the $\delta^{44/40}Ca$ record of the Lower Shale which is tentatively interpreted as inherited from the pre-dolomitisation carbonate material, although there is a negative correlation between $\delta^{44/40}Ca$ values and Mg/(Ca + Mg) ratios above the limestone bed in Unit IV (90.5–70 m; $R^2 = 0.40$, $p = 0.01$). However, the prominent positive excursion in $\delta^{44/40}Ca$ values in the middle of Unit IV (90.5 m) is associated with the appearance of a grey laminated limestone with abundant dissolution surfaces (Schneebeli-Hermann et al., 2020), and $\delta^{44/40}Ca$ values return to the pre-excursion values slightly above the top of the limestone bed. Several non-mutually exclusive mechanisms could explain this excursion. First, carbonates in the limestone bed may have experienced more fluid-buffered early diagenesis than the surrounding shale beds. Generally, shales have relatively low permeability, which can favour sediment-buffered conditions. In contrast, bioclastic limestones are often porous, which can promote recrystallisation under fluid-buffered conditions. Alternatively, if the limestone bed represents a hardground, the associated excursion in $\delta^{44/40}Ca$ values may reflect processes associated with extensive cement precipitation during hardground formation (Shinn, 1969; Erhardt et al., 2020). While these mechanisms cannot be distinguished at the present time, either could satisfactorily explain the $\delta^{44/40}Ca$ record of the Lower Shale.

5.2.3 | Unit V: *Tirolites* Limestone

The geochemical record of the *Tirolites* Limestone is interpreted as dominated by meteoric diagenetic processes. Geochemically, such processes are typified by (i) depleted trace-metal concentrations due to lower cation concentrations in fresh waters relative to sea water or sea water-derived fluids, (ii) lower $\delta^{13}C_{carb}$ values driven by DIC that partially originates from remineralised organic matter and (iii) lower $\delta^{18}O$ values inherited from precipitation, rather than sea water (Gross, 1964; Swart & Oehlert, 2018). In the Georgetown core, the *Tirolites* Limestone captures a sharp drop in $\delta^{13}C_{carb}$ values and several trace-metal ratios, particularly above 50 m (Figure 2). While $\delta^{13}C_{org}$ values do decline at this level, they quickly rebound and remain decoupled from $\delta^{13}C_{carb}$ values to the top of the Georgetown core. This variation has previously been interpreted as resulting from changes in the composition of sedimentary organic matter, rather than secular sea water DIC evolution (Schneebeli-Hermann et al., 2020). Given that this $\delta^{13}C_{carb}$ decline is not associated with large changes in $\delta^{44/40}Ca$ or $\delta^{26}Mg$ values, is not considered a global chemostratigraphic marker, but is associated with a well-known regional early Spathian regression (Vennin et al., 2015; Caravaca et al., 2017; Grosjean et al., 2018), meteoric diagenesis of the carbonate minerals is favoured as an explanation for this pattern. Some dolomite is also present in the *Tirolites* Limestone, but it is generally less abundant than in Units I–IV (Figure 2). These observations suggest that the dolomitisation process in the *Tirolites* Limestone preceded the onset of meteoric diagenesis.

While meteoric diagenesis is commonly associated with positive co-variation between $\delta^{13}C_{carb}$ and $\delta^{18}O$ values, no associated decline in $\delta^{18}O$ values is observed along with the $\delta^{13}C_{carb}$ decline. However, carbonate $\delta^{18}O$ values may reset by a variety of post-depositional processes. In the Georgetown core, $\delta^{18}O$ values were likely reset during subsequent burial diagenesis, which would significantly decrease carbonate $\delta^{18}O$ values. All Georgetown $\delta^{18}O$ values are lighter than Plio-Pleistocene carbonates that have clearly experienced meteoric diagenesis (Swart & Oehlert, 2018), as well as many time-equivalent carbonate successions (Payne et al., 2004). Sedimentologically, meteoric diagenesis is often associated with extensive karstification (Moore & Wade, 2013), which is observed throughout the *Tirolites* Limestone, providing an additional degree of support to the interpretation of a meteoric diagenetic control in the *Tirolites* Limestone.

5.2.4 | Summary

In the Georgetown core, the initial $\delta^{13}C_{carb}$ decline in the *Meekoceras* Limestone appears to reflect a transition from sediment-buffered to fluid-buffered early marine diagenesis, and the subsequent $\delta^{13}C_{carb}$ recovery and peak in the Lower Shale appear to capture a progressive decrease in the extent of dolomitisation. Likewise, the sharp drop in $\delta^{13}C_{carb}$ values in the *Tirolites* Limestone captures the influence of meteoric diagenesis. In short, the first-order control on the major excursions in $\delta^{13}C_{carb}$ values in the Georgetown core appear to be differing diagenetic styles, rather than secular change in the global carbon cycle. Even so, there are intervals in the Georgetown core that are less affected by post-depositional overprint than others—in

particular, the more sediment-buffered intervals at the base of Units I–III, and calcite-dominated samples in Unit IV. Based on those intervals, regional $\delta^{13}C_{DIC}$ values in the northern Sonoma Foreland Basin can be interpreted to have increased from *ca* 3‰ in the middle Smithian to *ca* 5‰ in the lower Spathian, although the timing and pathway through which $\delta^{13}C_{DIC}$ evolved cannot be definitively established within the core.

5.3 | Regional and global implications for the Smithian–Spathian boundary excursion

In the Georgetown core, the carbonate geochemistry of the Smithian–Spathian boundary interval appears to reflect variable diagenetic styles and processes, rather than global oceanic-atmospheric behaviour. While the paired $\delta^{13}C_{carb}$-$\delta^{13}C_{org}$ records of the Georgetown core are broadly comparable to others in the northern Sonoma subbasin (e.g., Hot Springs; Figure 1), they vary considerably from those in the southern Sonoma subbasin (Thomazo et al., 2016; Caravaca et al., 2017; Thomazo et al., 2019), suggesting that the presented interpretation of the Smithian–Spathian boundary excursion is applicable only to the northern Sonoma subbasin. Geochemical records and interpretations of the Smithian–Spathian boundary excursion also differ between the Panthalassan-influenced Sonoma Basin and other Tethys-influenced sections (Thomazo et al., 2016; Lyu et al., 2019; Zhang et al., 2019). Given their varied depositional settings, stratigraphic expressions and palaeoceanographic interpretations, several potential inconsistencies are outlined that may be re-assessed given the developing understanding of carbonate geochemistry across the Smithian–Spathian boundary interval.

5.3.1 | The Smithian–Spathian transition in the Sonoma Basin

In the northern Sonoma subbasin, the Hot Springs succession (Figure 8; Caravaca et al., 2017) serves as the main point of comparison for the Georgetown core. It is difficult to directly correlate Hot Springs to the Georgetown succession due to potential lithostratigraphic diachrony and/or stratigraphic contortion, along with considerable covered intervals in the former (see Caravaca et al., 2017; Schneebeli-Hermann et al., 2020 for further details). However, the Hot Springs sedimentological and paired $\delta^{13}C_{carb}$-$\delta^{13}C_{org}$ record is largely comparable to the Georgetown record. In the absence of carbonate-phase trace-metal and cation isotopic data from Hot Springs, it is hypothesised that its $\delta^{13}C_{carb}$ record may be driven by the same diagenetic processes as in Georgetown, suggesting some degree of regional consistency in diagenetic pathway and events throughout the northern Sonoma subbasin.

In contrast, differences emerge between the Georgetown succession and the southern Sonoma subbasin (Figure 8). There, Thomazo et al. (2016, 2019) examined a suite of geochemical proxies in the Mineral Mountains (Figure 1), where they recognised the characteristic Smithian–Spathian excursion in $\delta^{13}C_{carb}$ values with no associated excursion in $\delta^{13}C_{org}$ values. Based on $\delta^{34}S$ values from carbonate and pyrite phases, along with bulk trace-metal measurements, these workers suggested that the Smithian–Spathian boundary excursion primarily captured the cessation of bioturbation and associated authigenic carbonate precipitation, and in turn interpreted their observed $\delta^{13}C_{carb}$ trends as fundamentally local. In a similar vein, Decraene et al. (2023) employed coupled $\delta^{34}S_{pyrite}$ and $\delta^{56}Fe_{pyrite}$ values in Lower Weber Canyon (Figure 1, see also Grosjean et al., 2018) to suggest that a transition from open-system, oxic conditions to closed-system, anoxic conditions across the Smithian–Spathian boundary was again linked to changes in local depositional facies and authigenic carbonate precipitation, rather than global sea water evolution.

There is no direct geochemical evidence of anaerobic, authigenic dolomite precipitation (see Section 5.1.3) in the Georgetown core, although other styles of authigenic carbonate precipitation cannot be excluded. However, the most parsimonious interpretation of Georgetown carbonate geochemistry (see Section 5.2.4) does not invoke authigenic carbonate precipitation as a primary mechanistic driver. The sedimentological context of the Mineral Mountains and Georgetown successions may provide insight into why authigenic carbonate precipitation was more influential in the Mineral Mountains. The emergence of authigenic carbonate precipitation in the Mineral Mountains was linked to a transition from microbial and bioclastic-packstones to microbially-influenced mudstones, which Thomazo et al. (2016) linked to a reduction in the sedimentary mixed-layer. The sedimentary expression of the Thaynes Group, however, varies with palaeolatitude, and this sedimentological transition is not observed in the more-siliciclastic rich Georgetown succession. Therefore, widespread authigenic carbonate precipitation—at least of a consistent mechanistic style—is unlikely to satisfactorily explain the geochemical expression of the Smithian–Spathian boundary excursion throughout the entire Sonoma Basin. However, the geochemical expression of the Smithian–Spathian boundary excursion in the Sonoma Basin does appear to be largely influenced by diagenetic processes, even if diagenetic styles vary from section to section.

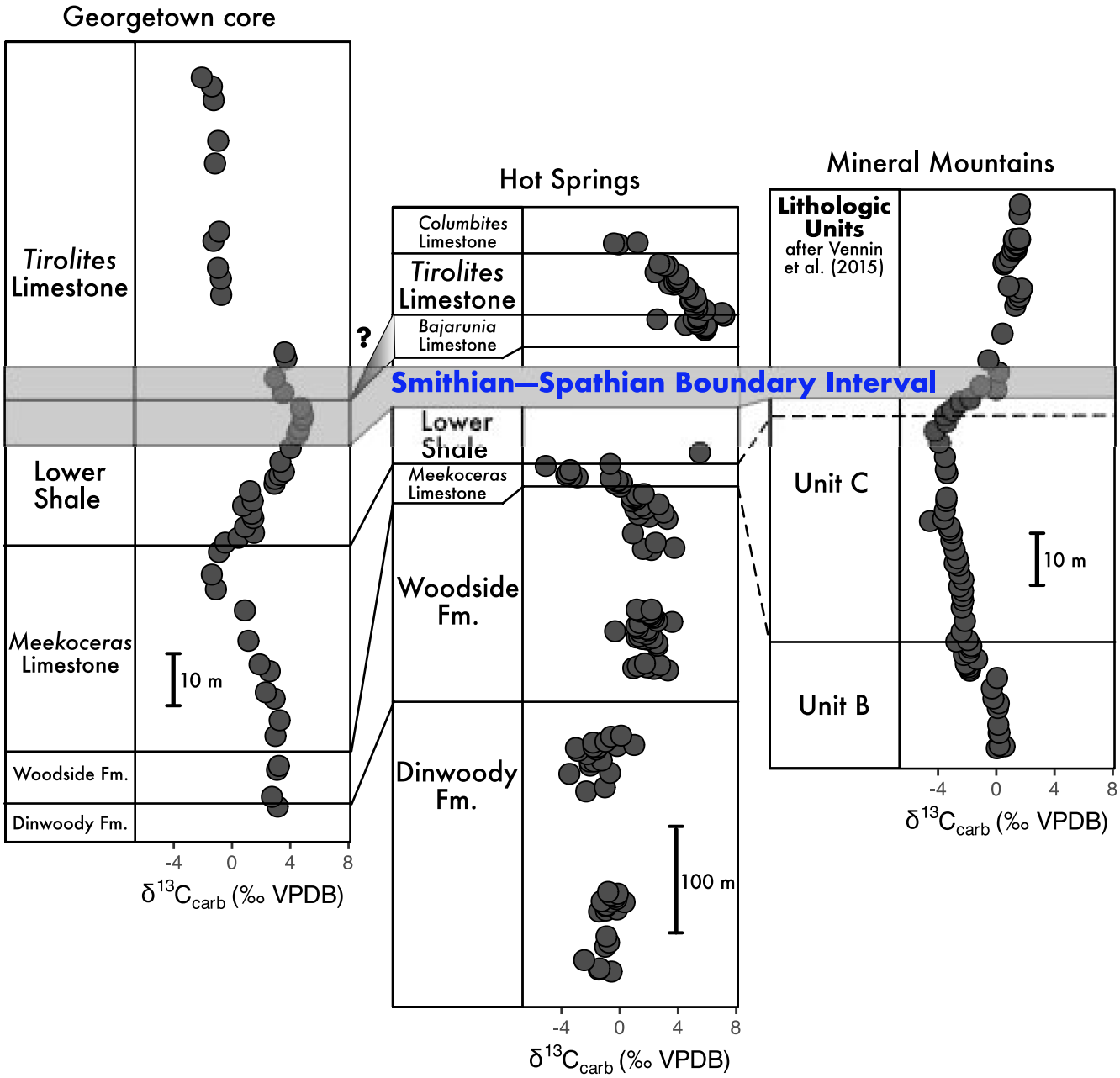

FIGURE 8 Chemostratigraphic $\delta^{13}C_{carb}$ profiles of regional Smithian–Spathian boundary successions in the Georgetown core, Hot Springs and the Mineral Mountains; refer to Figure 1 for section localities. Correlative lines between the Georgetown core and the Hot Springs section are based on lithostratigraphy. The dashed correlative lines between the Hot Springs and Mineral Mountains sections are based on ammonoid biostratigraphy, and do not imply lithostratigraphic equivalence. The absence of the *Bajarunia* Limestone in the Georgetown core is probably due to the lack of recovered diagnostic fauna, rather than a true unconformity, which may partially explain the observed diachrony at the basal *Tirolites* Limestone. In Hot Springs, stratigraphic and geochemical records are from Caravaca et al. (2017), but omitting the Permian portion of the succession. In the Mineral Mountains, stratigraphic and geochemical records are from Brayard et al. (2013), Vennin et al. (2015) and Thomazo et al. (2016, 2019).

5.3.2 | Global expression of the Smithian–Spathian transition

A variety of mechanisms have been proposed to explain the geochemical record of the Smithian–Spathian boundary interval, including changes in carbonate precipitation rates (Zhao et al., 2020b; Song et al., 2021; Ye et al., 2023), enhanced organic carbon burial (Galfetti et al., 2007b; Widmann et al., 2020), oceanic redox state (Algeo et al., 2019; Lyu et al., 2019; Zhang et al., 2019; Zhao et al., 2020a) and temperature (Goudemand et al., 2019; Song et al., 2019; Du et al., 2022). Here, our understanding of the carbonate record across the Smithian–Spathian boundary interval is assessed by focussing on studies with

calcium isotopic measurements and re-examining their proposed interpretations in view of the diagenetic frameworks outlined here.

In the Jiarong and Shitouzhai sections of southern China (Figure 8), Zhao et al. (2020b) observe that $\delta^{44/40}Ca$ values increase by 0.5–0.7‰ across the Smithian–Spathian boundary, concomitant with a 4–6‰ excursion in $\delta^{13}C_{carb}$ values, which they suggest could reflect either a local shift from 80% aragonitic to 80% calcitic primary minerology, or a 10–25× increase in global carbonate burial. They exclude the possibility of extensive early marine diagenesis due to the presence of a positive, rather than negative, co-variation between $\delta^{13}C_{carb}$ and $\delta^{44/40}Ca$. However, positive $\delta^{13}C_{carb}$-$\delta^{44/40}Ca$ co-variation is not inherently inconsistent with early marine diagenesis, as such trends exist in the geological record and are readily explained by early diagenetic models (Ahm et al., 2021; Busch et al., 2022). While a major shift in carbonate mineralogy across the boundary in the Jiarong and Shitouzhai sections cannot be excluded, the possibility that these sections record a transition from sediment-buffered to fluid-buffered diagenesis across the Smithian–Spathian boundary—rather than a global increase in carbonate burial—should be reconsidered.

Different $\delta^{44/40}Ca$ behaviours across the Smithian–Spathian boundary interval have been observed in other localities. For instance, in the Guryul Ravine section of Kashmir, Ye et al. (2023) observed that $\delta^{44/40}Ca$ values decrease by 0.2‰ across the Smithian–Spathian boundary, concomitant with a 10‰ excursion in $\delta^{13}C_{carb}$ values (Figure 8). Again, they suggest the geochemical record is not diagnostic of early marine diagenesis due to the absence of strong co-variation between $\delta^{44/40}Ca$ values and Mn/Sr, Mg/Ca or $\delta^{18}O$ values. They propose that this negative excursion in $\delta^{44/40}Ca$ values is associated with an up to 40% decrease in the carbonate burial flux across the Smithian–Spathian boundary, coupled with the spatially variable upwelling of acidic, anoxic water masses along the Palaeotethyan shelf (see also Song et al., 2021). These mechanisms rely on an assumption that the oceanic calcium reservoir was incompletely mixed on a regional scale, which seems unlikely in the absence of brackish conditions. However, that spatial variability in primary carbonate fractionation factors and/or diagenetic conditions due to variable palaeoceanographic conditions could drive observed $\delta^{44/40}Ca$ heterogeneity in the Smithian–Spathian boundary interval. While the suggested mechanisms of $\delta^{44/40}Ca$ evolution in the Georgetown core are different, they are consistent with Ye et al.'s (2023) suggestion that the regionally diverse $\delta^{44/40}Ca$ geochemical excursions recorded across the Smithian–Spathian boundary likely reflect spatially diverse conditions, capturing local geochemical dynamics rather than a globally-integrated signal.

The correlation and timing of the excursions in $\delta^{44/40}Ca$ values across the Smithian–Spathian boundary also challenge previous interpretations that their $\delta^{13}C$ records are associated with the evolution of the global DIC reservoir (Figure 9). In Jiarong, there is a sharp drop in $\delta^{44/40}Ca$ values across the Smithian–Spathian boundary, followed by a steady increase that is smaller than the magnitude of the pre-boundary $\delta^{44/40}Ca$ variability. In Shitouzhai, a steady increase in $\delta^{44/40}Ca$ values begins immediately before the Smithian–Spathian boundary, concurrent with the Smithian–Spathian boundary excursion. In Guryul Ravine, there is a very modest decline in $\delta^{44/40}Ca$ that begins before the boundary in association with the beginning of a positive excursion in $\delta^{13}C$ values, although the $\delta^{44/40}Ca$ variability is much more muted than elsewhere. Finally, in the Georgetown core $\delta^{44/40}Ca$ values increase well before the Smithian–Spathian boundary in association with lithologic changes and the nadir of the $\delta^{13}C_{carb}$ curve, with a second increase before the boundary associated with the recovery phase of the $\delta^{13}C_{carb}$ curve. The conodont biozonations in the Jiarong (Chen et al., 2015) and Guryul Ravine (Lyu et al., 2021) sections are based on extensive biostratigraphic sampling, and are considered to be stable. In contrast, the biostratigraphy of the Shitouzhai succession (Zhang et al., 2015) and the Georgetown core (Schneebeli-Hermann et al., 2020) are based on limited samples and, in the latter case, regional lithostratigraphic correlation, such that the biozone boundaries are somewhat uncertain and may be subject to change. However, the associated uncertainty in biostratigraphic correlation is relatively modest and unlikely to dramatically impact the implications of this study.

Taken as a whole, these observations suggest that carbonate geochemical records of the Smithian–Spathian boundary interval are substantially influenced by local controls, at least with regard to $\delta^{44/40}Ca$ values. Calcium is the major cation in carbonate rocks, is well-mixed throughout the ocean, and accordingly is considered to be one of the most resistant element to early marine diagenesis (Ahm et al., 2018; Lau & Hardisty, 2022). Consequently, the spatial and temporal heterogeneity of $\delta^{44/40}Ca$ values suggests that other carbonate-associated proxies across the Smithian–Spathian boundary transition are likely to be influenced by local and post-depositional conditions, and so may not necessarily capture a globally consistent signal of palaeoceanographic evolution. Given the wide variation in timing and magnitude of the Smithian–Spathian boundary excursion, the $\delta^{13}C$ records of this interval were likely modulated by local and post-depositional factors, as has been proposed in the Georgetown and Mineral Mountains successions (Thomazo et al., 2016). Careful, systematic work on carbonate geochemistry, coupled with a careful

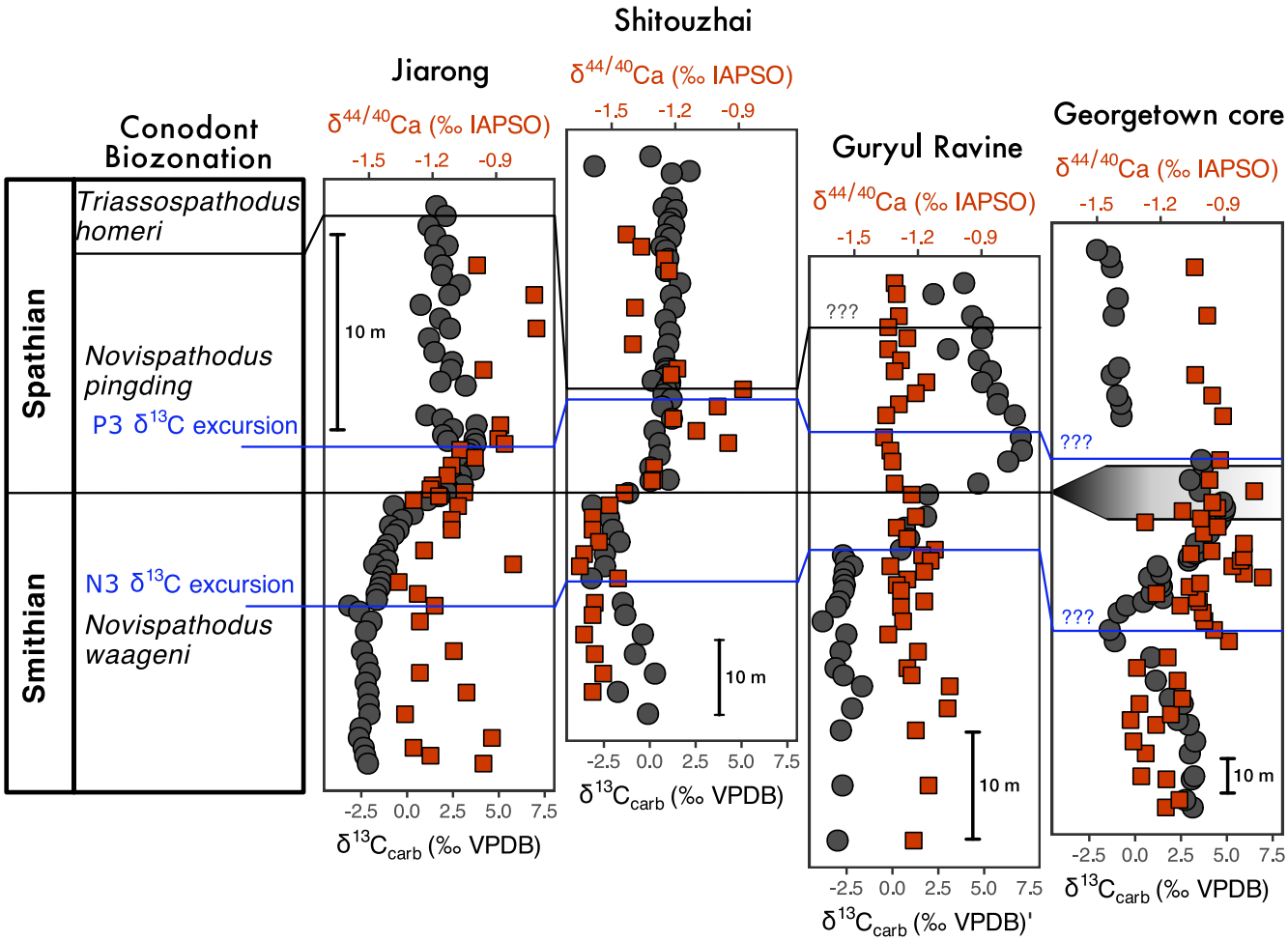

FIGURE 9 Stratigraphic comparison of $\delta^{13}C_{carb}$ and $\delta^{44/40}Ca$ profiles of notable Smithian–Spathian boundary successions in Jiarong, Shitouzhai, Guryul Ravine and the Georgetown core. The $\delta^{13}C_{carb}$, $\delta^{44/40}Ca$ and conodont records in Jiarong are from Lyu et al. (2019), Zhao et al. (2020b) and Chen et al. (2015), respectively. In Shitouzhai, $\delta^{13}C_{carb}$ records and conodont biozonations are from Zhang et al. (2015), while $\delta^{44/40}Ca$ are from Zhao et al. (2020b). In Guryul Ravine, $\delta^{13}C_{carb}$, $\delta^{44/40}Ca$ and conodont records are from Wang et al. (2019), Ye et al. (2023) and Lyu et al. (2021), respectively. The biostratigraphy of the Georgetown Core is based on palynology, scattered conodont and ammonoid recovery and lithostratigraphic correlation to regional sections with firm ammonoid zonation (Schneebeli-Hermann et al., 2020).

understanding of local depositional environments and post-depositional processes, is necessary for a complete mechanistic understanding of the geochemical evolution of the Smithian–Spathian boundary interval.

6 | CONCLUSION

The Smithian–Spathian boundary interval captures a pronounced positive excursion in $\delta^{13}C$ values, in concert with the widespread re-emergence of anachronistic facies, benthic ecological crises and pronounced extinction events across several major marine invertebrate clades. In this study, the geochemical evolution of the Smithian–Spathian boundary interval in the northern Sonoma subbasin is linked to local diagenetic processes—early marine diagenesis, anoxic dolomitisation and meteoric diagenesis—rather than directly reflecting global sea water evolution. Moreover, the style of diagenesis coincides with lithologic patterns, pointing to potential sedimentological controls on carbonate geochemistry and diagenesis. Based on a consideration of likely diagenetic mechanisms, a primary shift in local sea water DIC $\delta^{13}C$ values is inferred from the most geochemically unaltered strata, from about 3‰ in the middle Smithian to 5‰ in the early Spathian, although the timing and pathway through which this occurs cannot be readily identified nor extrapolated globally. Given the variable geochemical expression of the Smithian–Spathian boundary interval between individual sections and across depositional basins, and previous recognitions that aspects of this excursion may reflect local influences, the careful reconsideration of Smithian–Spathian boundary records to examine potential local and diagenetic influences is encouraged.

ACKNOWLEDGEMENTS

We kindly thank Roger Bryant for insightful comments during the preparation of this manuscript. JPT acknowledges support from an NSF Graduate Research Fellowship. This study was supported by a Society for Sedimentary Geology (SEPM) student research grant to JPT, NSF-EAR FRES grant #2120406 to CLB, and SNSF project #180253 to TV and HB. We thank Jon Husson and an anonymous reviewer for constructive reviews, and Peter Swart for editorial assistance that greatly improved this manuscript.

CONFLICT OF INTEREST STATEMENT

The authors declare no conflict of interest.

DATA AVAILABILITY STATEMENT

The data that support the findings of this study are available in the supplementary material of this article.

ORCID

Jordan P. Todes https://orcid.org/0000-0002-6043-3989

REFERENCES

Ahm, A.-S.C., Bjerrum, C.J., Blättler, C.L., Swart, P.K. & Higgins, J.A. (2018) Quantifying early marine diagenesis in shallow-water carbonate sediments. *Geochimica et Cosmochimica Acta*, 236, 140–159.

Ahm, A.-S.C., Bjerrum, C.J., Hoffman, P.F., Macdonald, F.A., Maloof, A.C., Rose, C.V., Strauss, J.V. & Higgins, J.A. (2021) The Ca and Mg isotope record of the Cryogenian Trezona carbon isotope excursion. *Earth and Planetary Science Letters*, 568, 117002.

Algeo, T.J., Brayard, A. & Richoz, S. (2019) The Smithian-Spathian boundary: a critical juncture in the Early Triassic recovery of marine ecosystems. *Earth-Science Reviews*,195, 1–6.

Banner, J.L. (1995) Application of the trace element and isotope geochemistry of strontium to studies of carbonate diagenesis. *Sedimentology*, 42, 805–824.

Banner, J.L. & Hanson, G.N. (1990) Calculation of simultaneous isotopic and trace element variations during water-rock interaction with applications to carbonate diagenesis. *Geochimica et Cosmochimica Acta*, 54, 3123–3137.

Blättler, C.L., Miller, N.R. & Higgins, J.A. (2015) Mg and Ca isotope signatures of authigenic dolomite in siliceous deep-sea sediments. *Earth and Planetary Science Letters*, 419, 32–42.

Bold, U., Ahm, A.-S.C., Schrag, D.P., Higgins, J.A., Jamsran, E. & Macdonald, F.A. (2020) Effect of dolomitization on isotopic records from Neoproterozoic carbonates in southwestern Mongolia. *Precambrian Research*, 350, 105902.

Brand, U. & Veizer, J. (1980) Chemical diagenesis of a multicomponent carbonate system; 1, Trace elements. *Journal of Sedimentary Research*, 50, 1219–1236.

Brayard, A., Bucher, H., Escarguel, G., Fluteau, F., Bourquin, S. & Galfetti, T. (2006) The Early Triassic ammonoid recovery: paleoclimatic significance of diversity gradients. *Palaeogeography, Palaeoclimatology, Palaeoecology*, 239, 374–395.

Brayard, A., Bylund, K.G., Jenks, J.F., Stephen, D.A., Olivier, N., Escarguel, G., Fara, E. & Vennin, E. (2013) Smithian ammonoid faunas from Utah: implications for Early Triassic biostratigraphy, correlation and basinal paleogeography. *Swiss Journal of Palaeontology*, 132, 141–219.

Brayard, A., Krumenacker, L.J., Botting, J.P., Jenks, J.F., Bylund, K.G., Fara, E., Vennin, E., Olivier, N., Goudemand, N., Saucède, T., Charbonnier, S., Romano, C., Doguzhaeva, L., Thuy, B., Hautmann, M., Stephen, D.A., Thomazo, C. & Escarguel, G. (2017) Unexpected Early Triassic marine ecosystem and the rise of the Modern evolutionary fauna. *Science Advances*, 3, e1602159.

Brayard, A., Meier, M., Escarguel, G., Fara, E., Nützel, A., Olivier, N., Bylund, K.G., Jenks, J.F., Stephen, D.A., Hautmann, M., Vennin, E. & Bucher, H. (2015) Early Triassic Gulliver gastropods: spatiotemporal distribution and significance for biotic recovery after the end-Permian mass extinction. *Earth-Science Reviews*, 146, 31–64.

Bryant, R.N., Present, T.M., Ahm, A.-S.C., McClelland, H.-L.O., Razionale, D. & Blättler, C.L. (2022) Early diagenetic constraints on Permian seawater chemistry from the Capitan Reef. *Geochimica et Cosmochimica Acta*, 328, 1–18.

Busch, J.F., Hodgin, E.B., Ahm, A.-S.C., Husson, J.M., Macdonald, F.A., Bergmann, K.D., Higgins, J.A. & Strauss, J.V. (2022) Global and local drivers of the Ediacaran Shuram carbon isotope excursion. *Earth and Planetary Science Letters*, 579, 117368.

Caravaca, G., Brayard, A., Vennin, E., Guiraud, M., Pourhiet, L.L., Grosjean, A.-S., Thomazo, C., Olivier, N., Fara, E., Escarguel, G., Bylund, K.G., Jenks, J.F. & Stephen, D.A. (2018) Controlling factors for differential subsidence in the Sonoma Foreland Basin (Early Triassic, western USA). *Geological Magazine*, 155, 1305–1329.

Caravaca, G., Thomazo, C., Vennin, E., Olivier, N., Cocquerez, T., Escarguel, G., Fara, E., Jenks, J.F., Bylund, K.G., Stephen, D.A. & Brayard, A. (2017) Early Triassic fluctuations of the global carbon cycle: new evidence from paired carbon isotopes in the western USA basin. *Global and Planetary Change*, 154, 10–22.

Chen, Y., Jiang, H., Lai, X., Yan, C., Richoz, S., Liu, X. & Wang, L. (2015) Early Triassic conodonts of Jiarong, Nanpanjiang Basin, southern Guizhou Province, South China. *Journal of Asian Earth Sciences*, 105, 104–121.

Corsetti, F.A., Baud, A., Marenco, P.J. & Richoz, S. (2005) Summary of Early Triassic carbon isotope records. *Comptes Rendus Palevol*, 4, 473–486.

Cramer, B.D. & Jarvis, I. (2020) Chapter 11—carbon isotope stratigraphy. In: Gradstein, F.M., Ogg, J.G., Schmitz, M.D. & Ogg, G.M. (Eds.) *Geologic Ttime Scale 2020*. Amsterdam, The Netherlands: Elsevier, pp. 309–343.

Crockford, P.W., Kunzmann, M., Blättler, C.L., Kalderon-Asael, B., Murphy, J.G., Ahm, A.-S., Sharoni, S., Halverson, G.P., Planavsky, N.J., Halevy, I. & Higgins, J.A. (2020) Reconstructing Neoproterozoic seawater chemistry from early diagenetic dolomite. *Geology*, 49, 442–446.

Decraene, M.-N., Marin-Carbonne, J., Thomazo, C., Brayard, A., Bouvier, A.-S., Bomou, B., Adatte, T. & Olivier, N. (2023) Pyrite iron isotope compositions track local sedimentation conditions through the Smithian-Spathian transition (Early Triassic, Utah, USA). *Palaeogeography, Palaeoclimatology, Palaeoecology*, 617, 111507.

DePaolo, D.J. (2011) Surface kinetic model for isotopic and trace element fractionation during precipitation of calcite from aqueous solutions. *Geochimica et Cosmochimica Acta*, 75, 1039–1056.

Derry, L.A. (2010) A burial diagenesis origin for the Ediacaran Shuram–Wonoka carbon isotope anomaly. *Earth and Planetary Science Letters*, 294, 152–162.

Derry, L.A., Kaufman, A.J. & Jacobsen, S.B. (1992) Sedimentary cycling and environmental change in the Late Proterozoic: evidence from stable and radiogenic isotopes. *Geochimica et Cosmochimica Acta*, 56, 1317–1329.

Du, Y., Song, H., Algeo, T.J., Song, H., Tian, L., Chu, D., Shi, W., Li, C. & Tong, J. (2022) A massive magmatic degassing event drove the Late Smithian Thermal Maximum and Smithian–Spathian boundary mass extinction. *Global and Planetary Change*, 215, 103878.

Erhardt, A.M., Turchyn, A.V., Bradbury, H.J. & Dickson, J.A.D. (2020) The calcium isotopic composition of carbonate hardground cements: a new record of changes in ocean chemistry? *Chemical Geology*, 540, 119490.

Fantle, M.S. & DePaolo, D.J. (2007) Ca isotopes in carbonate sediment and pore fluid from ODP Site 807A: the Ca^{2+}(aq)–calcite equilibrium fractionation factor and calcite recrystallization rates in Pleistocene sediments. *Geochimica et Cosmochimica Acta*, 71, 2524–2546.

Farkaš, J., Böhm, F., Wallmann, K., Blenkinsop, J., Eisenhauer, A., van Geldern, R., Munnecke, A., Voigt, S. & Veizer, J. (2007) Calcium isotope record of Phanerozoic oceans: implications for chemical evolution of seawater and its causative mechanisms. *Geochimica et Cosmochimica Acta*, 71, 5117–5134.

Galfetti, T., Bucher, H., Brayard, A., Hochuli, P.A., Weissert, H., Guodun, K., Atudorei, V. & Guex, J. (2007) Late Early Triassic climate change: insights from carbonate carbon isotopes, sedimentary evolution and ammonoid paleobiogeography. *Palaeogeography, Palaeoclimatology, Palaeoecology*, 243, 394–411.

Galfetti, T., Hochuli, P.A., Brayard, A., Bucher, H., Weissert, H. & Vigran, J.O. (2007) Smithian-Spathian boundary event: evidence for global climatic change in the wake of the end-Permian biotic crisis. *Geology*, 35, 291–294.

Geske, A., Zorlu, J., Richter, D.K., Buhl, D., Niedermayr, A. & Immenhauser, A. (2012) Impact of diagenesis and low grade metamorphosis on isotope (δ^{26}Mg, δ^{13}C, δ^{18}O and ^{87}Sr/^{86}Sr) and elemental (Ca, Mg, Mn, Fe and Sr) signatures of Triassic sabkha dolomites. *Chemical Geology*, 332–333, 45–64.

Goodspeed, T.H. & Lucas, S.G. (2007) Stratigraphy, sedimentology, and sequence stratigraphy of the Lower Triassic Sinbad Formation, San Rafael Swell, Utah. In: Lucas, S.G. & Spielmann, J.A. (Eds.) *Triassic of the American West: Bulletin 40*. Albuquerque, New Mexico, USA: New Mexico Museum of Natural History and Science.

Goudemand, N., Romano, C., Leu, M., Bucher, H., Trotter, J.A. & Williams, I.S. (2019) Dynamic interplay between climate and marine biodiversity upheavals during the early Triassic Smithian-Spathian biotic crisis. *Earth-Science Reviews*, 195, 169–178.

Grosjean, A.-S., Vennin, E., Olivier, N., Caravaca, G., Thomazo, C., Fara, E., Escarguel, G., Bylund, K.G., Jenks, J.F., Stephen, D.A. & Brayard, A. (2018) Early Triassic environmental dynamics and microbial development during the Smithian–Spathian transition (Lower Weber Canyon, Utah, USA). *Sedimentary Geology*, 363, 136–151.

Gross, M.G. (1964) Variations in the O^{18}/O^{16} and C^{13}/C^{12} Ratios of Diagenetically Altered Limestones in the Bermuda Islands. *The Journal of Geology*, 72, 170–194.

Higgins, J.A., Blättler, C.L., Lundstrom, E.A., Santiago-Ramos, D.P., Akhtar, A.A., Crüger Ahm, A.-S., Bialik, O., Holmden, C., Bradbury, H., Murray, S.T. & Swart, P.K. (2018) Mineralogy, early marine diagenesis, and the chemistry of shallow-water carbonate sediments. *Geochimica et Cosmochimica Acta*, 220, 512–534.

Higgins, J.A. & Schrag, D.P. (2010) Constraining magnesium cycling in marine sediments using magnesium isotopes. *Geochimica et Cosmochimica Acta*, 74, 5039–5053.

Hu, Z., Hu, W., Wang, X., Lu, Y., Wang, L., Liao, Z. & Li, W. (2017) Resetting of Mg isotopes between calcite and dolomite during burial metamorphism: outlook of Mg isotopes as geothermometer and seawater proxy. *Geochimica et Cosmochimica Acta*, 208, 24–40.

Hu, Z., Li, W., Zhang, H., Krainer, K., Zheng, Q., Xia, Z., Hu, W. & Shen, S. (2021) Mg isotope evidence for restriction events within the Paleotethys ocean around the Permian-Triassic transition. *Earth and Planetary Science Letters*, 556, 116704.

Husson, J.M., Higgins, J.A., Maloof, A.C. & Schoene, B. (2015) Ca and Mg isotope constraints on the origin of Earth's deepest δ^{13}C excursion. *Geochimica et Cosmochimica Acta*, 160, 243–266.

Jacobson, A.D. & Holmden, C. (2008) δ^{44}Ca evolution in a carbonate aquifer and its bearing on the equilibrium isotope fractionation factor for calcite. *Earth and Planetary Science Letters*, 270, 349–353.

Jenkyns, H.C. (1975) Origin of Red Nodular Limestones (Ammonitico Rosso, Knollenkalke) in the Mediterranean Jurassic: a Diagenetic Model. In: *Pelagic sediments: on Land and under the Sea*. Oxford, United Kingdom: John Wiley & Sons, Ltd, pp. 249–271.

Kennedy, W.J. & Garrison, R.E. (1975) Morphology and genesis of nodular chalks and hardgrounds in the Upper Cretaceous of southern England. *Sedimentology*, 22, 311–386.

Klinkhammer, G.P. (1980) Early diagenesis in sediments from the eastern equatorial Pacific, II. Pore water metal results. *Earth and Planetary Science Letters*, 49, 81–101.

Knoll, A.H., Hayes, J.M., Kaufman, A.J., Swett, K. & Lambert, I.B. (1986) Secular variation in carbon isotope ratios from Upper Proterozoic successions of Svalbard and East Greenland. *Nature*, 321, 832–838.

Komar, N. & Zeebe, R.E. (2011) Oceanic calcium changes from enhanced weathering during the Paleocene-Eocene thermal maximum: no effect on calcium-based proxies. *Paleoceanography*, 26. PA321.https://doi.org/10.1029/2010PA001979

Komar, N. & Zeebe, R.E. (2016) Calcium and calcium isotope changes during carbon cycle perturbations at the end-Permian. *Paleoceanography*, 31, 115–130.

Korte, C., Kozur, H.W. & Veizer, J. (2005) δ^{13}C and δ^{18}O values of Triassic brachiopods and carbonate rocks as proxies for coeval seawater and palaeotemperature. *Palaeogeography, Palaeoclimatology, Palaeoecology*, 226, 287–306.

Kummel, B. (1943) The Thaynes Formation, Bear Lake Valley, Idaho. *American Journal of Science*, 241, 316–332.

Kummel, B. (1954) Triassic stratigraphy of Southeastern Idaho and adjacent areas. *Geological Survey Professional Paper*, 254-H, 165–199.

Lau, K.V. & Hardisty, D.S. (2022) Modeling the impacts of diagenesis on carbonate paleoredox proxies. *Geochimica et Cosmochimica Acta*, 337, 123–139.

Li, W., Beard, B.L., Li, C., Xu, H. & Johnson, C.M. (2015) Experimental calibration of Mg isotope fractionation between dolomite and

aqueous solution and its geological implications. *Geochimica et Cosmochimica Acta*, 157, 164–181.

Lucas, S.G., Krainer, K. & Milner, A.R.C. (2007) The type section and age of the Timpoweap Member and stratigraphic nomenclature of the Triassic Moenkopi Group in southwestern Utah. In: Lucas, S.G. & Spielmann, J.A. (Eds.) *Triassic of the American West: Bulletin 40*. Albuquerque, New Mexico, USA: New Mexico Museum of Natural History and Science.

Lyu, Z., Orchard, M.J., Golding, M.L., Henderson, C.M., Chen, Z.-Q., Zhang, L., Han, C., Wu, S., Huang, Y., Zhao, L., Bhat, G.M. & Baud, A. (2021) Lower Triassic conodont biostratigraphy of the Guryul Ravine section, Kashmir. *Global and Planetary Change*, 207, 103671.

Lyu, Z., Zhang, L., Algeo, T.J., Zhao, L., Chen, Z.-Q., Li, C., Ma, B. & Ye, F. (2019) Global-ocean circulation changes during the Smithian–Spathian transition inferred from carbon-sulfur cycle records. *Earth-Science Reviews*, 195, 114–132.

Meyer, K.M., Yu, M., Jost, A.B., Kelley, B.M. & Payne, J.L. (2011) $\delta^{13}C$ evidence that high primary productivity delayed recovery from end-Permian mass extinction. *Earth and Planetary Science Letters*, 302, 378–384.

Meyer, K.M., Yu, M., Lehrmann, D., van de Schootbrugge, B. & Payne, J.L. (2013) Constraints on Early Triassic carbon cycle dynamics from paired organic and inorganic carbon isotope records. *Earth and Planetary Science Letters*, 361, 429–435.

Moore, C.H. & Wade, W.J. (2013) Chapter 8—Meteoric Diagenetic Environment. In: Moore, C.H. & Wade, W.J. (Eds.) *Developments in Sedimentology*, Vol. 67. Amsterdam, The Netherlands: Elsevier, pp. 165–206.

Mueller, M., Igbokwe, O.A., Walter, B., Pederson, C.L., Riechelmann, S., Richter, D.K., Albert, R., Gerdes, A., Buhl, D., Neuser, R.D., Bertotti, G. & Immenhauser, A. (2020) Testing the preservation potential of early diagenetic dolomites as geochemical archives. *Sedimentology*, 67, 849–881.

Nelson, L.L., Ahm, A.-S.C., Macdonald, F.A., Higgins, J.A. & Smith, E.F. (2021) Fingerprinting local controls on the Neoproterozoic carbon cycle with the isotopic record of Cryogenian carbonates in the Panamint Range, California. *Earth and Planetary Science Letters*, 566, 116956.

Oehlert, A.M. & Swart, P.K. (2014) Interpreting carbonate and organic carbon isotope covariance in the sedimentary record. *Nature Communications*, 5, 4672.

Payne, J.L. & Kump, L.R. (2007) Evidence for recurrent Early Triassic massive volcanism from quantitative interpretation of carbon isotope fluctuations. *Earth and Planetary Science Letters*, 256, 264–277.

Payne, J.L., Lehrmann, D.J., Wei, J., Orchard, M.J., Schrag, D.P. & Knoll, A.H. (2004) Large Perturbations of the Carbon Cycle During Recovery from the End-Permian Extinction. *Science*, 305, 506–509.

Razionale, D., Bryant, R.N. & Blättler, C.L. (2022) Adapting automated instrumentation for high-throughput calcium isotope measurements by multi-collector inductively coupled plasma mass spectrometry. *Rapid Communications in Mass Spectrometry*, 36, e9249.

Romano, C., Jenks, J.F., Jattiot, R., Scheyer, T.M., Bylund, K.G. & Bucher, H. (2017) Marine Early Triassic Actinopterygii from Elko County (Nevada, USA): implications for the Smithian equatorial vertebrate eclipse. *Journal of Paleontology*, 91, 1025–1046.

Saenger, C. & Wang, Z. (2014) Magnesium isotope fractionation in biogenic and abiogenic carbonates: implications for paleoenvironmental proxies. *Quaternary Science Reviews*, 90, 1–21.

Saltzman, M.R. & Sedlacek, A.R.C. (2013) Chemostratigraphy indicates a relatively complete Late Permian to Early Triassic sequence in the western United States. *Geology*, 41, 399–402.

Schneebeli-Hermann, E., Bagherpour, B., Vennemann, T., Leu, M. & Bucher, H. (2020) Sedimentary organic matter from a cored Early Triassic succession, Georgetown (Idaho, USA). *Swiss Journal of Palaeontology*, 139, 5.

Schrag, D.P., Higgins, J.A., Macdonald, F.A. & Johnston, D.T. (2013) Authigenic carbonate and the history of the global carbon cycle. *Science*, 339, 540–543.

Shinn, E.A. (1969) Submarine lithification of Holocene carbonate sediments in the Persian Gulf. *Sedimentology*, 12, 109–144.

Shinn, E.A., Robbin, D.M., Lidz, B.H. & Hudson, J.H. (1983) Influence of deposition and early diagenesis on porosity and chemical compaction in two Paleozoic buildups: Mississippian and Permian age rocks in the Sacramento Mountains, New Mexico. In: Harris, P.M. (Ed.) *Carbonate buildups—a core workshop*, Vol.4. Tulsa, Oklahoma, USA: Tulsa, Oklahoma, USA: SEPM Society for Sedimentary Geology, pp. 182–222.

Smith, C.P.A., Laville, T., Fara, E., Escarguel, G., Olivier, N., Vennin, E., Goudemand, N., Bylund, K.G., Jenks, J.F., Stephen, D.A., Hautmann, M., Charbonnier, S., Krumenacker, L.J. & Brayard, A. (2021) Exceptional fossil assemblages confirm the existence of complex Early Triassic ecosystems during the early Spathian. *Scientific Reports*, 11, 19657.

Solien, M.A. (1979) Conodont Biostratigraphy of the Lower Triassic Thaynes Formation, Utah. *Journal of Paleontology*, 53, 276–306.

Song, H., Du, Y., Algeo, T.J., Tong, J., Owens, J.D., Song, H., Tian, L., Qiu, H., Zhu, Y. & Lyons, T.W. (2019) Cooling-driven oceanic anoxia across the Smithian/Spathian boundary (mid-Early Triassic). *Earth-Science Reviews*, 195, 133–146.

Song, H., Song, H., Tong, J., Gordon, G.W., Wignall, P.B., Tian, L., Zheng, W., Algeo, T.J., Liang, L., Bai, R., Wu, K. & Anbar, A.D. (2021) Conodont calcium isotopic evidence for multiple shelf acidification events during the Early Triassic. *Chemical Geology*, 562, 120038.

Swart, P.K. (2015) The geochemistry of carbonate diagenesis: the past, present and future. *Sedimentology*, 62, 1233–1304.

Swart, P.K. & Oehlert, A.M. (2018) Revised interpretations of stable C and O patterns in carbonate rocks resulting from meteoric diagenesis. *Sedimentary Geology*, 364, 14–23.

Swart, P.K., Oehlert, A.M., Mackenzie, G.J., Eberli, G.P. & Reijmer, J.J.G. (2014) The fertilization of The Bahamas by Saharan dust: a trigger for carbonate precipitation? *Geology*, 42, 671–674.

Tang, J., Dietzel, M., Böhm, F., Köhler, S.J. & Eisenhauer, A. (2008) Sr^{2+}/Ca^{2+} and $^{44}Ca/^{40}Ca$ fractionation during inorganic calcite formation: II. Ca isotopes. *Geochimica et Cosmochimica Acta*, 72, 3733–3745.

Tang, J., Köhler, S.J. & Dietzel, M. (2008) Sr^{2+}/Ca^{2+} and $^{44}Ca/^{40}Ca$ fractionation during inorganic calcite formation: I. Sr incorporation. *Geochimica et Cosmochimica Acta*, 72, 3718–3732.

Tebo, B.M. (1991) Manganese(II) oxidation in the suboxic zone of the Black Sea. *Deep Sea Research Part A. Oceanographic Research Papers*, 38, S883–S905.

Thomazo, C., Brayard, A., Elmeknassi, S., Vennin, E., Olivier, N., Caravaca, G., Escarguel, G., Fara, E., Bylund, K.G., Jenks, J.F.,

Stephen, D.A., Killingsworth, B., Sansjofre, P. & Cartigny, P. (2019) Multiple sulfur isotope signals associated with the late Smithian event and the Smithian/Spathian boundary. *Earth-Science Reviews*, 195, 96–113.

Thomazo, C., Vennin, E., Brayard, A., Bour, I., Mathieu, O., Elmeknassi, S., Olivier, N., Escarguel, G., Bylund, K.G., Jenks, J., Stephen, D.A. & Fara, E. (2016) A diagenetic control on the Early Triassic Smithian–Spathian carbon isotopic excursions recorded in the marine settings of the Thaynes Group (Utah, USA). *Geobiology*, 14, 220–236.

Vennin, E., Olivier, N., Brayard, A., Bour, I., Thomazo, C., Escarguel, G., Fara, E., Bylund, K.G., Jenks, J.F., Stephen, D.A. & Hofmann, R. (2015) Microbial deposits in the aftermath of the end-Permian mass extinction: a diverging case from the Mineral Mountains (Utah, USA). *Sedimentology*, 62, 753–792.

Wang, X., Cawood, P.A., Zhao, H., Zhao, L., Grasby, S.E., Chen, Z.-Q. & Zhang, L. (2019) Global mercury cycle during the end-Permian mass extinction and subsequent Early Triassic recovery. *Earth and Planetary Science Letters*, 513, 144–155.

Widmann, P., Bucher, H., Leu, M., Vennemann, T., Bagherpour, B., Schneebeli-Hermann, E., Goudemand, N. & Schaltegger, U. (2020) Dynamics of the largest carbon isotope excursion during the Early Triassic biotic recovery. *Frontiers in Earth Science*, 8, 196.

Xia, Z., Horita, J., Reuning, L., Bialik, O.M., Hu, Z., Waldmann, N.D., Liu, C. & Li, W. (2020) Extracting Mg isotope signatures of ancient seawater from marine halite: a reconnaissance. *Chemical Geology*, 552, 119768.

Xia, Z., Li, S., Hu, Z., Bialik, O., Chen, T., Weldeghebriel, M.F., Fan, Q., Fan, J., Wang, X., An, S., Zhang, F., Xu, H., Chen, J., Ji, Z., Shen, S., Lowenstein, T.K. & Li, W. (2024) The evolution of Earth's surficial Mg cycle over the past 2 billion years. *Science Advances*, 10, eadj5474.

Ye, F., Zhao, L., Zhang, L., Cui, Y., Algeo, T.J., Chen, Z.-Q., Lyu, Z., Huang, Y., Bhat, G.M. & Baud, A. (2023) Calcium isotopes reveal shelf acidification on southern Neotethyan margin during the Smithian-Spathian boundary cooling event. *Global and Planetary Change*, 227, 104138.

Young, E.D., Galy, A. & Nagahara, H. (2002) Kinetic and equilibrium mass-dependent isotope fractionation laws in nature and their geochemical and cosmochemical significance. *Geochimica et Cosmochimica Acta*, 66, 1095–1104.

Zhang, L., Orchard, M.J., Brayard, A., Algeo, T.J., Zhao, L., Chen, Z.-Q. & Lyu, Z. (2019) The Smithian/Spathian boundary (late Early Triassic): a review of ammonoid, conodont, and carbon-isotopic criteria. *Earth-Science Reviews*, 195, 7–36.

Zhang, L., Zhao, L., Chen, Z.-Q., Algeo, T.J., Li, Y. & Cao, L. (2015) Amelioration of marine environments at the Smithian–Spathian boundary, Early Triassic. *Biogeosciences*, 12, 1597–1613.

Zhang, S. & DePaolo, D.J. (2020) Equilibrium calcite-fluid Sr/Ca partition coefficient from marine sediment and pore fluids. *Geochimica et Cosmochimica Acta*, 289, 33–46.

Zhao, H., Algeo, T.J., Liu, Y., Chen, Z.-Q., Zhang, L., Hu, Z. & Li, Z. (2020) Lower Triassic carbonate $\delta^{238}U$ record demonstrates expanded oceanic anoxia during Smithian thermal maximum and improved ventilation during Smithian-Spathian boundary cooling event. *Palaeogeography, Palaeoclimatology, Palaeoecology*, 539, 109393.

Zhao, H., Dahl, T.W., Chen, Z.-Q., Algeo, T.J., Zhang, L., Liu, Y., Hu, Z. & Hu, Z. (2020) Anomalous marine calcium cycle linked to carbonate factory change after the Smithian Thermal Maximum (Early Triassic). *Earth-Science Reviews*, 211, 103418.

SUPPORTING INFORMATION

Additional supporting information can be found online in the Supporting Information section at the end of this article.

How to cite this article: Todes, J.P., Blattmann, F.R., Vennemann, T., Schneebeli-Hermann, E., Bucher, H., Razionale, D.P. et al. (2024) Smithian–Spathian carbonate geochemistry in the northern Thaynes Group influenced by multiple styles of diagenesis. *The Depositional Record*, 00, 1–21. Available from: https://doi.org/10.1002/dep2.321